J. Fluid Mech. (2015), *vol.* 769, *pp.* 242–276. © Cambridge University Press 2015
doi:10.1017/jfm.2015.128

Microstructure and rheology relationships for shear thickening colloidal dispersions

A. Kate Gurnon[1] **and Norman J. Wagner**[1,†]

[1]Center for Neutron Science, Department of Chemical and Biomolecular Engineering, University of Delaware, Newark, DE 19716, USA

(Received 29 May 2014; revised 21 February 2015; accepted 23 February 2015; first published online 16 March 2015)

The non-Newtonian shear rheology of colloidal dispersions is the result of the competition and balance between hydrodynamic (dissipative) and thermodynamic (conservative) forces that lead to a non-equilibrium microstructure under flow. We present the first experimental measurements of the shear-induced microstructure of a concentrated near-hard-sphere colloidal dispersion through the shear thickening transition using small-angle neutron scattering (SANS) measurements made in three orthogonal planes during steady shear. New instrumentation coupled with theoretical derivations of the stress-SANS rule enable rigorous testing of the relationship between this non-equilibrium microstructure and the observed macroscopic shear rheology. The thermodynamic and hydrodynamic components of the stress that drive shear thinning, shear thickening and first normal stress differences are separately defined via stress-SANS rules and compared to the rheological behaviour of the dispersion during steady shear. Observations of shear-induced hydrocluster formation is in good agreement with Stokesian dynamics simulation results by Foss & Brady (*J. Fluid Mech.*, vol. 407, 2000, pp. 167–200). This unique set of measurements of shear rheology and non-equilibrium microstructure of a model system provides new insights into suspension mechanics as well as a method to rigorously test constitutive equations for colloidal suspension rheology.

Key words: colloids, rheology, suspensions

1. Introduction

Concentrated hard-sphere colloidal dispersions subjected to increasing shear stress display a reversible rise in viscosity with increasing shear rate known as shear thickening (Hoffman 1974; Barnes 1989; Bender & Wagner 1996). Shear thickening colloidal suspensions have the potential to be implemented in a wide variety of applications. In recent research these shear thickening fluids (STFs) have been investigated for applications such as personal protective armour (Lee, Wetzel & Wagner 2003; David, Gao & Zheng 2009; Kalman *et al.* 2009), medical devices and sports equipment (Helber, Doncker & Bung 1990; Fischer *et al.* 2007). STFs also find application in vibrating systems to reduce resonance amplitudes (Helber *et al.*

† Email address for correspondence: wagnernj@udel.edu

1990), as interlayers of sandwich beam structures (Fischer *et al.* 2007) and as a 'speed-activated' damper under dynamic loadings (Helber *et al.* 1990; Zhang, Li & Gong 2008). Mitigating shear thickening has proven equally critical for a broad range of industries from coatings to cement production (Toussaint, Roy & Jezequel 2009) and chemical mechanical planarization of semiconductors (Crawford *et al.* 2013). All of these applications require a fundamental understanding of the colloidal dispersion's reversible thinning and thickening behaviour and underlying microstructure during shear flow.

Suspension stresses are calculated as ensemble averages of the forces acting between particles, where the spatial arrangement of the particles, or microstructure, is represented by the pair distribution function (Batchelor & Green 1972; Batchelor 1977). Thus, the non-Newtonian shear behaviour of concentrated colloidal suspensions is intimately linked to the microstructure changes that occur when the suspension is forced out of equilibrium during shear. The total measured stress comprises components derived from conservative or thermodynamic forces, such as Brownian motion and interparticle forces, and those arising from dissipative sources, such as hydrodynamic interactions. These two classes of force couple to the structure differently to yield the stress tensor, such that measurements of the structure provide a unique method to determine structure–property relationships in colloidal dispersions (Wagner, Fuller & Russel 1988; Mewis & Wagner 2011). Consequently, it is essential to understand quantitatively this microstructure under flow in order to predict the behaviour of STFs and facilitate rational design and formulation of concentrated colloidal suspensions for commercial and industrial applications. Two directions of scientific discovery drive the research dedicated to understanding the microstructure–rheology property relationship of concentrated colloidal suspensions. The first is theoretical and simulation-driven research using the Smoluchowski equation and Stokesian dynamics simulations of Brownian hard-sphere suspensions (Bossis & Brady 1989; Wagner & Ackerson 1992; Foss & Brady 2000; Bergenholtz, Brady & Vicic 2002; Melrose & Ball 2004; Nazockdast & Morris 2013). The second is experimental measures of a colloidal dispersion's microstructure during shear deformation (Wagner *et al.* 1988; D'Haene, Mewis & Fuller 1993; Bender & Wagner 1996; Maranzano & Wagner 2002; Kalman 2010; Cheng *et al.* 2011*a*; Xu & Gilchrist 2014). The two methods are by no means mutually exclusive and often, as is the case here, they complement each other.

Of significant interest to many investigating shear thickening colloidal dispersions is identifying the microstructure responsible for the shear thinning and thickening behaviour. Initially, simultaneous flow and small-angle light scattering (SALS) experiments were performed by Hoffman (1974) in the 1–2 plane of shear, where an order-to-disorder transition was observed at the onset of shear thickening. The formation of ordered layers of particles parallel to the velocity direction and normal to the velocity gradient direction formed under low shear rates, and as the shear rate increased the layers were observed to break up into a randomized structure. Although Hoffman (1974) was the first to offer a significant microstructure–rheology relationship for shear thickening, the order–disorder transition has since been shown not to be a prerequisite for shear thickening, as confirmed by Stokesian dynamics simulations (Bossis & Brady 1989) and experimental results (Laun *et al.* 1992; D'Haene *et al.* 1993; Bender & Wagner 1995, 1996).

The reversible shear thickening observed in colloidal suspensions is driven by short-range lubrication interactions that lead to density fluctuations of particles during shear and, ultimately, to particle clustering (termed 'hydroclusters' by Brady & Bossis

(1985, 1988) and Maranzano & Wagner (2002)). The development of the technique of Stokesian dynamics simulations for Brownian suspensions properly accounted for both the short-range lubrication interactions and long-range hydrodynamics, including many-body interactions (Brady & Bossis 1985; Brady & Vicic 1995). The results of these simulations showed particle cluster formation due to lubrication interactions between particles through the suspending fluid (Bossis & Brady 1989; Phung, Brady & Bossis 1996; Foss & Brady 2000; Banchio & Brady 2003; Melrose & Ball 2004). The most accurate set of calculations for the viscosity as a function of increasing shear rate was performed by Banchio & Brady (2003) using accelerated Stokesian dynamics simulations. Equally important, shear thickening due to shear-induced density fluctuations of particles is also predicted from theory that properly includes the short-range lubrication hydrodynamic interactions (Bergenholtz *et al.* 2002; Nazockdast & Morris 2013).

Recently, shear thickening in non-colloidal suspensions has been studied by combining classical methods of macroscopic contact friction adapted from granular mechanics with suspension hydrodynamics (Seto *et al.* 2013; Mari *et al.* 2014). Simulations can capture many features of continuous and discontinuous shear thickening, and it has been suggested that such surface friction may be relevant for shear thickening in colloidal dispersions (Mari *et al.* 2014). Modelling the transition from a hydrodynamically dominated regime to a frictional regime can yield multiple, coexisting stress states that provide a possible mechanism for discontinuous shear thickening observed in dilatant suspensions (Cates & Wyart 2014). However, one can rule out any significant role of contact friction in the continuous shear thickening of colloidal dispersions, as contact friction leads to the incorrect sign of the first normal stress difference, which is measured to be negative in the shear thickened state (Lee *et al.* 2006; Mewis & Wagner 2011; Cwalina & Wagner 2014) but predicted to be positive for systems with frictional contacts (Mari *et al.* 2014). Indeed, this negative first normal stress difference is a hallmark of suspensions dominated by hydrodynamics (see Mewis & Wagner (2011, chap. 2) for a review and Morris & Boulay (1999) for theory), and is predicted for shear thickening colloidal suspensions using Stokesian dynamics simulations by Foss & Brady (2000) and via theory by Bergenholtz *et al.* (2002), in agreement with experiments. This positive normal stress difference is a direct consequence of fore–aft symmetry breaking in the plane of shear and is well understood for systems with interparticle forces and frictional contacts alike. Finally, it is important to note that most colloidal dispersions are typically stabilized by adsorbed or grafted surfactant or polymer (such as for the dispersions under consideration here (Kalman & Wagner 2009)), and direct measurements of the friction for such surfaces show extremely low coefficients of friction (in the range from 0.0006 to 0.001 as reported by Klein and co-workers (Raviv *et al.* 2003)), whereas values close to unity are assumed in the simulations showing shear thickening (Mari *et al.* 2014). Indeed, direct measurements of colloidal friction coefficients by Henderson, Mitchell & Bartlett (2001) using optical tweezers quantitatively agreed with predictions of colloidal hydrodynamics. Only under the most extreme pressures, such that stabilizing brushes are highly compressed, are order-one coefficients of friction achieved (Raviv *et al.* 2003). Importantly, very high impact stress measurements of shear thickening colloidal suspensions in confinement (Lim *et al.* 2010*a*,*b*, 2011) show a response that is consistent with elastohydrodynamics, i.e. due to lubrication hydrodynamics coupled to the elastic deformation of the core hard colloidal particles (Kalman *et al.* 2009; Mewis & Wagner 2011). Indeed, increasing the adsorbed or grafted polymer layer thickness, which would increase contact friction

according to surface force measurements but mitigate lubrication hydrodynamics, all but eliminates shear thickening in colloidal dispersions (Krishnamurthy, Wagner & Mewis 2005). This brief review of the evidence concerning friction in colloidal dispersions provides context for the differences in shear-induced microstructures measured by experiment and simulated for frictional non-colloidal suspensions, which will be shown here as well through experimental determination of the structure in the relevant plane of shear along with the rheological functions.

Wagner & Ackerson (1992) derived the relationship between the microstructure measurable in a scattering experiment and the suspension stress for colloidal dispersions through a spherical harmonic expansion of the microstructure during shear flow, which provides a rigorous micromechanical basis for stress-optical (Wagner *et al.* 1988; Bender & Wagner 1995) and stress-SANS rules (Maranzano & Wagner 2002). Specifically, they derived a quantitative relationship between the flow-distorted microstructure and the stresses arising from the Brownian and hydrodynamic interactions. Importantly, it was found that the contribution of Brownian forces to the stress can be distinguished from the contributions from hydrodynamic interactions as arising from distinct terms in the spherical harmonic expansion of the microstructure. A similar approach was employed by Bergenholtz *et al.* (2002) to calculate the microstructure and stresses for a dilute colloidal dispersion. This theoretical work provides the basis for an important avenue of experimental investigations into the fundamentals of colloidal dispersion rheology because deconvolution of the shearing microstructure enables calculations of the contributions of conservative forces (e.g. Brownian and interparticle) and dissipative forces (e.g. hydrodynamic and frictional) to the total macroscopic suspension stress.

Small-angle neutron scattering (SANS) experiments have also been used to examine colloidal suspensions (Ackerson *et al.* 1986; Johnson, deKruif & May 1988; deKruif, Van der Werff & Johnson 1990; Laun *et al.* 1992; Bender & Wagner 1996; Watanabe *et al.* 1998; Newstein *et al.* 1999; Maranzano & Wagner 2002; Lee & Wagner 2006). In particular, Maranzano & Wagner (2002) and Lee & Wagner (2006) use rheo-SANS to investigate the microstructure in the tangential and radial planes of shear, resulting in quantitative resolution of the hydrodynamic contribution from the microstructure to the total stress. Ultra-SANS (USANS) experiments conducted by Kalman & Wagner (2009) probe the microstructure of a hard-sphere suspension in the velocity–velocity gradient plane of shear for which increased structure formation is observed during shear flow. Although these flow-USANS measurements provided important information about the scale and spatial organization of hydroclusters in a shear thickening suspension, the data obtained are one-dimensional (1D), so that inversion to determine the real-space structural anisotropy is not possible. Finally, Kalman and co-workers were the first to investigate the formation of hydroclusters in the velocity–velocity gradient plane of shear using SANS experiments (Kalman 2010). The results for the microstructure agree qualitatively with predictions from Stokesian dynamics simulation for the real-space pair distribution function during shear flow (Foss & Brady 2000). In addition, these experiments provide key results towards establishing a stress-SANS rule for colloidal suspensions measured using flow-SANS experiments. Thus, an understanding of the relationship between the rheology and microstructure of colloidal suspensions is established based on the independent contributions to the total stress arising from hydrodynamic and thermodynamic forces. For completeness, we note that flow-SALS (Wagner *et al.* 1988) and flow-SAXS (small-angle X-ray scattering) have also been used to probe colloidal dispersions, specifically the work by Hoekstra *et al.* (2005) as well as Versmold *et al.* (2001)

and Versmold, Musa & Bierbaum (2002). However, for colloidal suspensions, SAXS proves to be difficult, as multiple scattering and background scattering are problematic for concentrated suspensions.

Most recently, efforts using fast confocal microscopy have provided direct visualization of colloidal suspensions during shear. Besseling *et al.* (2009) successfully demonstrate three-dimensional (3D) imaging of a colloidal glass under steady shear, while Cohen, Mason & Weitz (2004) and Cheng *et al.* (2011*a*,*b*) use confocal microscopy to look at the effects of confinement on suspensions of colloidal particles and the microstructure responsible for the shear thinning and shear thickening rheology. Gao *et al.* (2010) study the microstructure of colloidal suspensions in pressure-driven flows. Cheng *et al.* (2011*a*) use confocal microscopy to elucidate the microscopic single-particle dynamics, concluding, in agreement with previous work, that shear thinning is a result of a decreasing relative contribution of entropic forces and that shear thickening arises from particle clustering induced by hydrodynamic interactions. Cheng *et al.* (2011*a*,*b*) observe 'log-rolling' strings of particles normal to the plane of shear for experiments that have a maximum gap between the shear plates of 10.6 times the diameter of a particle. Based on previous work by Cohen *et al.* (2004), significant confinement effects are present at this particular gap height that influence the microstructure. Cheng *et al.* (2011*b*) perform a systematic study using Stokesian dynamics simulations to address the mechanism for the 'log-rolling'-like structure that is observed for high *Pe*. Three key observations are made: the first is that, if there are no hydrodynamic interactions, there is no vorticity-aligned structure, and strings form along the velocity direction of shear; the second is that, if slip is introduced at the particle–fluid interface, a qualitatively similar, vorticity-aligned microstructure is observed; finally, the vorticity-aligned strings do not form when there is only one particle layer. These observations suggest that, in order to form strings in the vorticity direction, both thermodynamic and hydrodynamic interactions are important, and it is critical for particles to be able to migrate across different layers in the velocity gradient direction during shear. In addition, the small gap widths used in the experiments (of the order of 10 particle diameters) prove to have significant effects on the measured microstructure of the flowing suspension (see also Bian *et al.* 2014). Although useful for defining single-particle dynamics, the confocal microscopy is limited in resolution to particle sizes of the order of a micrometre. Because of limits on positional resolution, such methods are critically unable to resolve the lubrication layer essential for shear thickening.

In the present paper, the microstructure of a concentrated colloidal suspension is measured using rheo-SANS and flow-SANS methods to interrogate all three orthogonal planes of a 3D microstructure formed during steady shear for length scales spanning the interesting region of particle nearest neighbours. The resultant two-dimensional (2D) scattering patterns are presented for shear rates at moderate and high *Pe*, corresponding to shear thinning and shear thickening behaviour. The scattering patterns are also analysed and discussed to provide insight into the 3D microstructure of a flowing suspension under shear. The first quantitative analysis of all three planes of scattering for a concentrated colloidal suspension undergoing steady shear deformation is presented, and the microstructure contributions to the hydrodynamic and thermodynamic stresses are resolved. We employ the spherical harmonic expansion of the structure factor by Wagner & Ackerson (1992) to systematically deconvolute the 2D patterns by weighted interpretations and averaging over the most relevant length scales to identify the microstructural components that most significantly contribute to the stresses. Stress-SANS coefficients for the

	Symbol	Value	Units
Volume fraction	ϕ	0.40	—
d-EG density	$\rho_{d\text{-}EG}$	1.234	g ml^{-1}
PEG-600 density	$\rho_{PEG\text{-}600}$	1.125	g ml^{-1}
Particle density	ρ_p	1.89	g ml^{-1}
Particle core radius	a	61.1	nm
Shell thickness	t	1.65	nm
Suspending fluid viscosity	η_f	0.04	Pa s
Polydispersity		8	%
Scattering length density difference	$\Delta\rho_{sld}$	0.482×10^{-6}	Å^{-2}
Relative zero-shear viscosity	$\eta_{r,0}$	25.4	—
Relative high-shear viscosity	$\eta_{r,\infty}$	7.97	—
Relative high-frequency viscosity	$\eta'_{r,\infty}$	5.90	—
Effective hard-sphere volume fraction	ϕ_{eff}	0.465	—
Average relaxation time	λ_{ave}	0.045	s

TABLE 1. Summary of suspension properties.

hydrodynamic and thermodynamic components are defined by comparing stresses determined by the microstructure to the measured stresses. These results agree well with the suspension's rheology during steady shear and to accelerated Stokesian dynamics simulation results by Foss & Brady (2000).

2. Experimental methods and materials

2.1. *Materials*

A concentrated near-hard-sphere colloidal suspension comprising silica particles ($r =$ 61.1 nm) with polydispersity of 8 % ($\rho = 1.89$ g ml^{-1}), which were purchased in powder form (Seahoster Co., LLC, Japan). The particles are suspended at a particle loading volume fraction of 0.40 (for which the effective volume fraction is $\phi_{eff} =$ 0.465; figure 1) in a mixture of deuterated ethylene glycol (d-EG) (68 vol.%) and polyethylene glycol, $M_w = 600$ (PEG-600) (32 vol.%). The suspension is placed on a roll mixer for 72 h prior to experiments (table 1).

2.2. *Rheometry*

The suspension shear rheology is measured using an ARES-G2 strain-controlled rheometer measured with a 1° cone-and-plate geometry equipped with Peltier plate temperature control. The suspension is placed on the Peltier plate, the upper tool is lowered to the gap height and the sample is trimmed. The measurement protocol starts with a pre-shear consisting of 60 s of 10 s^{-1} steady shear rate and then steady shear-rate sweeps increasing and decreasing from 0.1 to 500 s^{-1}; this protocol is repeated eight times. The purpose of such an extensive pre-shear method is twofold: the first is to erase any shear history induced by loading the sample; and the second is to break up any remaining aggregates of particles in suspension that were not fully dispersed during the 72 h of roll mixing. After this pre-shear protocol, the steady shear rheology is measured from 0.1 to 500 s^{-1} (again increasing and decreasing in shear rate), where at each shear rate the suspension equilibrates to a constant shear

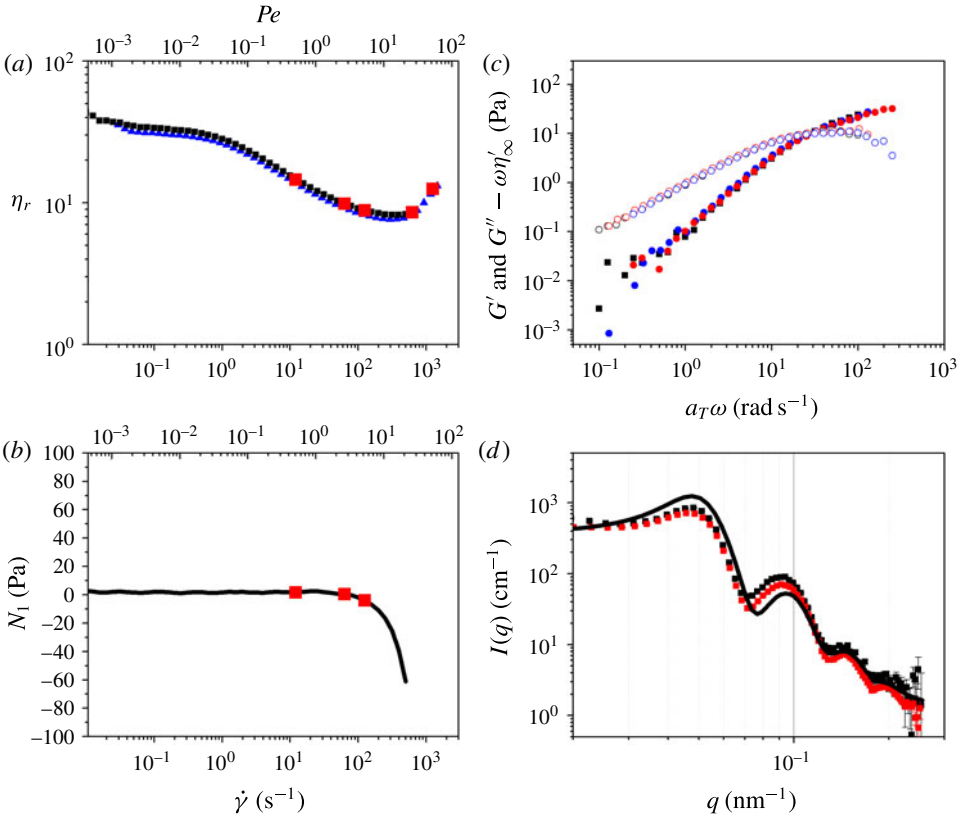

FIGURE 1. (Colour online) (*a*) Steady shear viscosity and (*b*) first normal stress as functions of shear rate and *Pe*: small black points/line, 5 °C; small grey points/line (blue online), 25 °C; large squares (red online) taken as peak holds at rheo-SANS conditions. (*c*) Linear viscoelastic moduli as a function of frequency for constant $\gamma_0 = 0.05$: filled symbols, G'; open symbols, $G'' - \omega\eta'_\infty$; greyscale (colours) correspond to 5 °C (black), 15 °C (mid-grey, red online) and 25 °C (dark grey, blue online). (*d*) The 1D SANS $I(q)$ as a function of q (nm^{-1}) for 5 mm pathlength flow-SANS shear cell (grey squares, red online) and 2 mm pathlength rheo-SANS Couette geometry (black squares) at equilibrium. The black line is a core–shell hard-sphere model for $\phi = 0.40$, $a = 611$ nm and shell thickness $t = 1.65$ nm (table 1).

response for 30 s. The steady shear and linear viscoelastic rheology is measured at three temperatures ($T = 5$, 15 and 25 °C). Time–temperature superposition (TTS) according to the analysis methods by Shikata & Pearson (1994) defines the steady shear and linear viscoelastic rheology reported in figure 1(*a–c*) for which $T_{ref} = 25$ °C.

The dimensionless Péclet number (*Pe*) is the dimensionless shear rate defined as the ratio of the shear rate to the rate of diffusion by Brownian motion in the dilute limit, and is used to compare with simulations and theory:

$$Pe = \frac{6\pi\eta_f a^3\dot{\gamma}}{k_B T}. \tag{2.1}$$

2.3. *Small-angle neutron scattering (SANS)*

Rheo- and flow-SANS experiments were performed at the Institute Laue-Langevin, Grenoble, France, on the D-22 SANS beamline. For the three different shear sample environments (radial-, tangential- and flow-SANS), the sample-to-detector distance is 17.6 m, the wavelength is 10 Å and the slit dimension is 0.5 mm. Rheo-SANS experiments were performed to measure the SANS scattering in the radial direction interrogating the velocity–vorticity (1–3) plane and the tangential direction to interrogate the velocity gradient–vorticity (2–3) plane during shear flow. These experiments were conducted using an Anton Paar 501 rheometer with quartz Couette geometry to apply a steady shear flow (Porcar *et al.* 2011). Measurements in the velocity–velocity gradient (1–2) plane of shear were performed using a flow-SANS sample environment (Gurnon *et al.* 2014). Scattering data are presented in terms of the scattering vector $\boldsymbol{q}$ or its amplitude $|\boldsymbol{q}| = q = 4\pi \sin(\theta/2)/\lambda$, where θ is the scattering angle. Data were reduced to an absolute scale using GRASP (Dewhurst 2011) and the subsequent application of the weighting functions to each reduced 2D dataset is performed using SASET (Muthig *et al.* 2013).

3. Results and discussion

The steady shear measurements in figure 1(*a*) show the typical shear thinning and shear thickening response of a concentrated colloidal suspension undergoing increasing steady shear flow. From the steady shear rheology, we define the zero-shear viscosity ($\eta_{r,0} = 25.4$) and the high-shear viscosity ($\eta_{r,\infty} = 7.97$), which is taken as the viscosity minimum. Comparison to hard-sphere theory (Russel, Wagner & Mewis 2013) defines the effective hard-sphere volume fraction to be $\phi_{eff} = 0.465$ (table 1). Figure 1(*b*) presents the first normal stress difference of the suspension during steady shear flow. In agreement with other measures of $N_1(\dot{\gamma})$ by Cwalina & Wagner (2014) during shear thinning, the first normal stress is slightly positive and then becomes increasingly negative as the shear rate increases during shear thickening.

Figure 1(*c*) shows the linear viscoelastic moduli of the suspension for three different temperatures shifted using TTS and subtracting the purely viscous contribution to the loss modulus to define the linear viscoelastic moduli G' and $G'' - \omega\eta'_\infty$ as a function of frequency. The suspension's relaxation time is identified as the inverse of the cross-over frequency ($\lambda = 1/\omega$), reported in table 1 as $\lambda = 0.045$ s.

Figure 1(*d*) shows a core–shell hard-sphere model fit to 1D quiescent scattering data in the rheo- and flow-SANS sample environments using the parameters in table 1. The corresponding structure factor is reported in figure 2(*a*). The effective volume fraction calculated from the core–shell model is 0.468, which agrees well with the effective volume fraction from the rheology reported in table 1. The maximum in the structure factor occurs at slightly larger q than the peak in the intensity $I(q)$. The maximum in the structure factor corresponds to the length scale for nearest-neighbour interactions shaded in figure 2, where $q_{peak} = 0.042$–0.064 nm^{-1}, corresponding to length scales of 100–150 nm.

3.1. *SANS scattering results in three planes during steady shear flow*

Rheo- and flow-SANS microstructure measurements of a concentrated colloidal dispersion are reported for experiments made in all three planes during steady shear flow. Figure 3(*a*,*b*) shows those results from measurements made in the velocity–velocity gradient (1–2) plane of shear. The 2D scattering results are reported

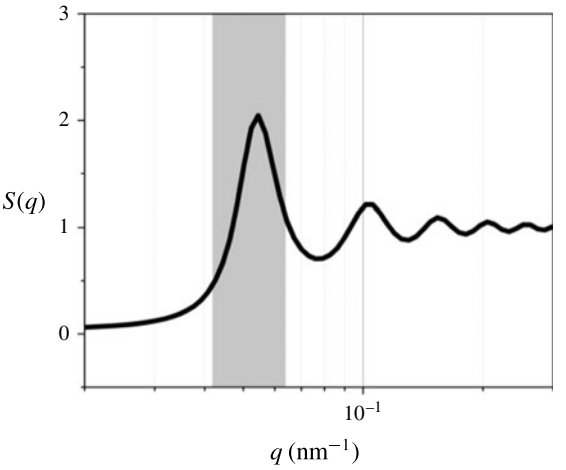

FIGURE 2. Hard-sphere structure factor, $S(q)$, where $q_{peak} = 0.0546$ nm^{-1} for $\phi = 0.40$ and $a = 61.1$ nm. The shaded portion corresponds to the nearest-neighbour peak ($q_{peak} = 0.042$–0.064 nm^{-1}).

for increasing shear rates from left to right. The second row reports subtracted 2D scattering patterns, where the equilibrium scattering (figure 3, left) has been subtracted from the scattering measured during shear, thus highlighting changes upon applying shear flow. We begin by observing that the anisotropic features of the scattering grow in intensity with increasing shear rate, indicating that shear distorts the dispersion's microstructure. The experimental coordinate system is given in the figure, and it is important to recognize the inherent inverse relationship between reciprocal-space scattering patterns and the real-space microstructure, such that the scattering patterns correspond to a 90° rotation of the real-space structure. The increased intensity observed with increasing shear rate in the 2D scattering patterns is oriented along the extension axis, such that particle neighbours are enhanced along the compression axis of the shear flow. This experimental result is consistent with that previously reported in work by Kalman (2010) and predicted using Stokesian dynamics simulations by Foss & Brady (2000) and via theory by Bergenholtz *et al.* (2002). In the velocity–velocity gradient plane of shear, our scattering experiments show a real-space microstructure under shear for which an increased number of nearest neighbours exist along the compression axis of shear and a depletion of neighbouring particles along the extension axis.

Scattering results from experiments in the velocity–vorticity (1–3) plane during shear flow are shown in figure 3(*b*). Just as in the 1–2 plane, the increasing SANS scattered intensity is an indication of microstructure changes increasing with increasing shear rate. The experiment is such that the neutron beam passes through the sample twice. Therefore, in the velocity–vorticity plane, under laminar flow the microstructure should have mirror symmetry across the vorticity and velocity axes. Shear-induced structure is evident as in increasing intensity for low q along the direction of shear. An interpretation of this increased intensity under shear relative to equilibrium is of a preferential organization of particles along the vorticity axis. Previous experiments by Cheng *et al.* (2011*a*) using confocal microscopy have observed similar structures that they define as 'chaining' along the vorticity direction.

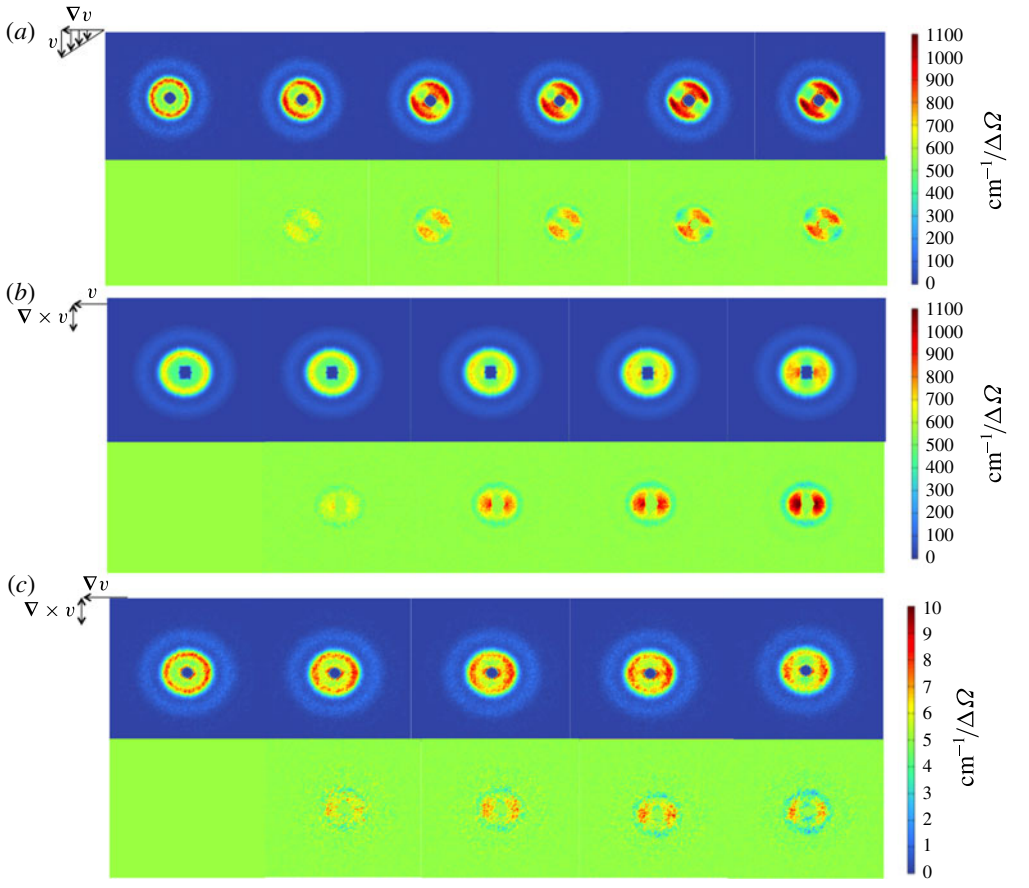

FIGURE 3. Flow-SANS 2D scattering patterns (upper row) and subtracted patterns (lower row) for which the equilibrium scattering (at $\dot{\gamma} = 0$) is subtracted from the scattering measured during shear: (*a*) the velocity–velocity gradient plane, (*b*) the velocity–vorticity plane, and (*c*) the vorticity–velocity gradient plane. From left to right $\dot{\gamma} = 0$, 12, 63, 125, 627, and 1258 s^{-1}, with the highest shear rate only measured for the velocity–velocity gradient plane.

The measurements in the velocity gradient–vorticity (2–3) plane are reported as figure 3(*c*). These rheo-SANS experiments are also performed in the Couette sample environment by alignment of the beam tangential to the Couette cell. As a consequence, there is a loss of resolution due to both the increase in pathlength, leading to multiple scattering, as well as sampling over curved streamlines. Nevertheless, a qualitative comparison of these results also shows increasing scattering with increasing shear rate. As observed for the 1–3 plane, here again we observe structure and apparent alignment along the vorticity direction of shear flow.

The three planes interrogated with the rheo- and flow-SANS experiments reported here are orthogonal to one another and provide the first scattering measurements in all three planes of flow spanning the shear thinning and shear thickening transition. From these, we can build an understanding of the 3D real-space microstructure that exists for a concentrated colloidal suspension during steady shear.

Figure 4 presents a direct comparison between predictions for the pair distribution function $g(\boldsymbol{r})$ from accelerated Stokesian dynamics simulations by Foss & Brady (2000) for a concentrated suspension of hard-sphere particles at a comparable concentration ($\phi = 0.45$) and those experimental results for $I(\boldsymbol{q})$ from the SANS experiments presented in the previous section for the velocity–velocity gradient (1–2), velocity–vorticity (1–3) and velocity gradient–vorticity (2–3) planes during shear. The upper row in each panel of figure 4 shows the Stokesian dynamic simulations, where the lighter regions indicate a higher probability for finding a particle at that location in the shear flow. The best resolution using Stokesian dynamics simulations reported in the figures is around the nearest-neighbour (i.e. innermost) ring. Longer length-scale structures are resolved by SANS experiments presented in the 2D scattering patterns in the lower row of each panel in figure 4. For reference, black circles are superimposed on the scattering patterns to delineate the q range corresponding to the nearest-neighbour position, as identified in figure 2.

Good qualitative agreement is observed for the microstructures simulated and measured, especially for the velocity–velocity gradient plane shown in the upper rows in each panel of figure 4. In particular, there are clear increases in the intensity with increasing shear rate along the compression axis of shear on length scales associated with nearest neighbours. Furthermore, at the highest shear rates, we observe particularly good agreement at the $\sim 0^\circ$ and $\sim 180^\circ$ positions, where brighter spots of intensity are evident in both simulation and experiment. The scattering observed from the 1–2 plane of shear identifies the signature hydrocluster microstructure of colloidal dispersions (Kalman 2010). These hydroclusters have been shown to be the result of density fluctuations caused by applying a shear of significant rate to a colloidal suspension such that the particles become strongly coupled by lubrication hydrodynamic interactions acting in the thin fluid layer between particles driven close together. This results in an increase in energy dissipated, reflected in the bulk stress response of the shear thickening suspension. The hydroclusters have been shown to form with structure along the compression axis of shear in previous flow-SANS experiments by Kalman (2010) as well as predicted by Stokesian dynamics simulations by Foss & Brady (2000). In these experiments, we observe that hydroclusters are evident on longer length scales, which are associated with q values inside the smallest circle superimposed over the 2D scattering pattern. The experiments here further corroborate these findings, where in the 1–2 plane particles associate with one another primarily along the compression axis, which contributes to the increase in the stress observed during bulk rheometry experiments as a shear thickening response.

A comparison between Stokesian dynamics simulation results and flow-SANS experiments in the velocity–vorticity plane is presented in figure 4. Interestingly, for length scales associated with the nearest-neighbour ring (as those predicted by Stokesian dynamics (Foss & Brady 2000)), the SANS and simulation results both show only slight changes in scattering intensity associated with nearest-neighbour interactions (highlighted in the SANS patterns by the black circles). The largest changes in scattering upon shear observed in the 1–3 plane occur at longer length scales (at low q values). Note that these structures are not readily detected in the real-space pair distribution functions calculated by Stokesian dynamics, because these second- and third-nearest-neighbour correlations are washed out and of low amplitude relative to the nearest-neighbour correlations. Such larger length-scale structures are readily apparent in scattering measurements, however, corresponding to smaller q values (inside of the smallest circle in figure 4). This observation suggests that the

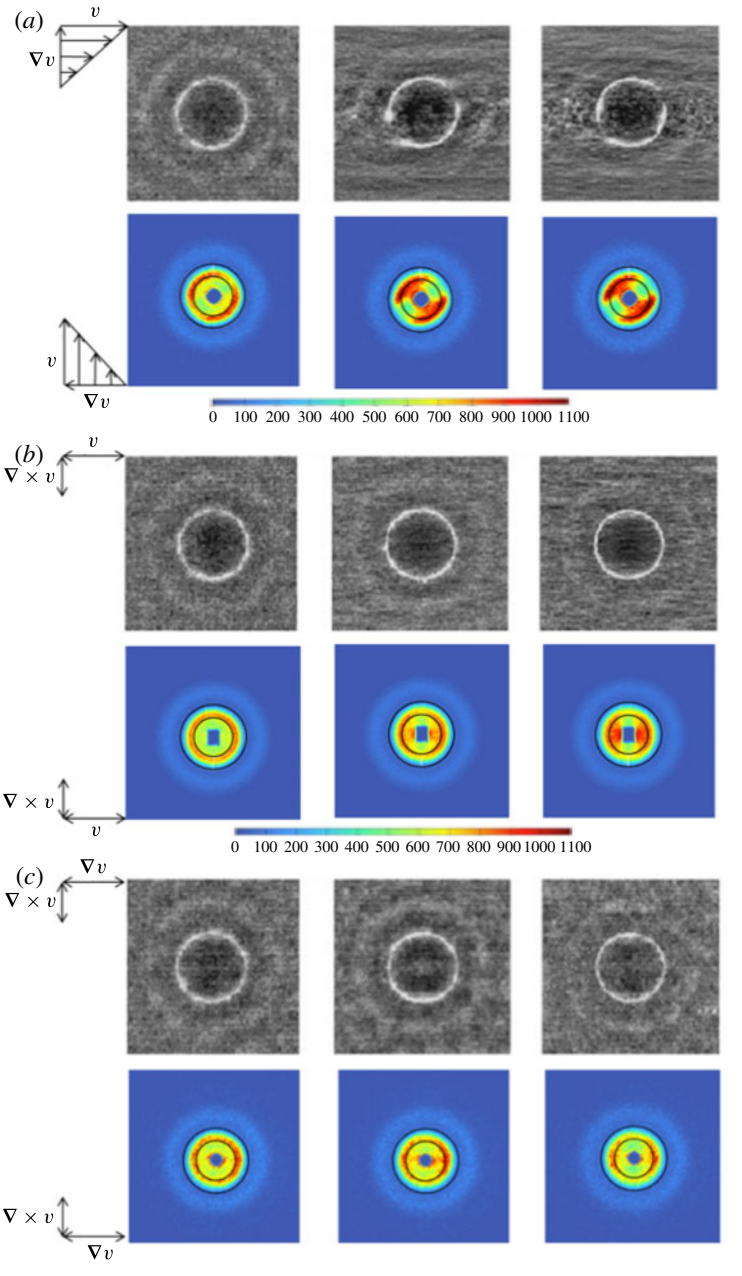

FIGURE 4. Comparison of Stokesian dynamics simulations with SANS results for: (*a*) velocity–velocity gradient, (*b*) velocity–vorticity, and (*c*) velocity gradient–vorticity planes of shear. In each panel the upper row shows the corresponding projection of $g(r)$ from Stokesian dynamics simulations from Foss & Brady (2000) for $Pe = 0.43$, 10 and 100, where lighter colours are indicative of higher concentration of particles, darker colours are lower concentration. The lower row of each panel shows SANS pattern from flow-SANS experiments for $Pe = 0.52$, 5.23 and 52.6, where warmer colours are indicative of more scattering events and cooler colours are fewer scattering events according to the scale bar to the right. The black circles indicate the nearest-neighbour peak in the structure factor from figure 2 for $q_{peak} = 0.042$–0.064 nm^{-1}.

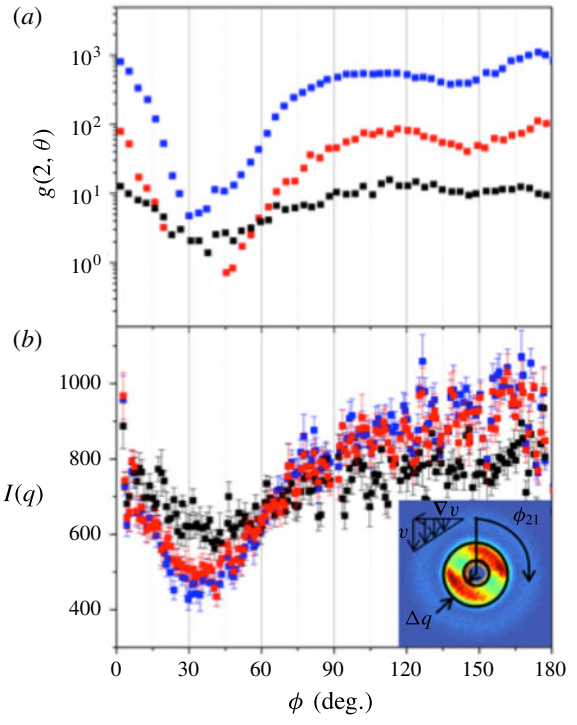

FIGURE 5. (Colour online) (*a*) Plot of $g(r, \theta)$ from accelerated Stokesian dynamics simulations from Foss & Brady (2000) for $Pe = 1$ (black square), 25 (mid-grey square; red online) and 1000 (dark grey square; blue online). (*b*) Plot of $I(q, \phi_{21} + 90°)$ for $Pe = 2.62$ (black square), 26.2 (mid-grey square; red online) and 52.6 (dark grey square; blue online) for $\dot{\gamma} = 12$, 627 and 1258 s^{-1}). The abscissa in both cases is the angle ϕ as defined in the inset.

anisotropy detected in the SANS scattering patterns is from larger microstructures associated with correlations spanning multiple particles. The increased intensity indicates that there is a preference for particles to align along the vorticity direction. The scattering patterns reveal structures for length scales corresponding to three to four particle diameters, as reported previously for hydrocluster formation by Kalman & Wagner (2009). Associations across multiple particles in the vorticity direction, which grow with increasing shear, give rise to the SANS scattering patterns in the 1–3 plane. This vorticity alignment is also evident in the velocity gradient–vorticity (2–3) plane scattering, although the patterns suffer from a longer scattering pathlength and lower resolution. These scattering patterns indicate that particles are preferentially aligned along the vorticity plane during shear with increasing shear rate. The particle alignment along the vorticity direction of shear has been observed using confocal microscopy experiments and Stokesian dynamics simulations by Cheng *et al.* (2011*a*,*b*), which suggest that the particle chaining observed along the vorticity direction is caused by hydrodynamic interactions, where particles migrate across the velocity gradient direction of shear flow.

The qualitative comparison shows that many key features of the colloidal microstructure elucidated by our measurements in all three planes of symmetry

by scattering are captured in the Stokesian dynamics simulations. These measured structures can be quantitatively used to understand the rheological response through micromechanical relationships that account for hydrodynamic interactions. Differences in our measured microstructures and those recently reported for non-colloidal suspensions with friction further serve to highlight the importance of colloidal hydrodynamics in shear thickening colloidal dispersions. Mari *et al.* (2014) show that the structure in the discontinuous shear thickened state in the plane of shear becomes more isotropic, whereas the measured microstructure of the colloidal suspension develops a very distinct and prominent anisotropy under shear flow that is most evident in the plane of flow (velocity–gradient plane). As discussed in the introduction, this difference may be due in part to the very low coefficient of friction under high loads for organically coated particles such as those used here (reported to be 0.08) in comparison to the high friction reported for bare SiO_2 particles (0.39; Kappl *et al.* 2006). The quantitative link between the measured microstructures for shear thickening colloidal dispersions and the measured mechanical stresses are presented and discussed in the next section in the context of colloidal hydrodynamics.

3.2. *Microstructure–stress relationship*

The stress-SANS rule establishes a quantitative connection between the flowing microstructure measured using SANS and the stress response of a complex fluid during shear (Maranzano & Wagner 2002). This is accomplished via a spherical harmonic expansion of the 3D microstructure given in (3.1) (Wagner & Ackerson 1992). Importantly, for colloidal dispersions, the stress and microstructure both have contributions from two fundamentally separate, but equally important, forces: thermodynamic (superscript T) and hydrodynamic (superscript H). This section will discuss the systematic methods used to describe the total shear stress (superscript σ) and normal stress (superscript N_1) response of the suspension and define the stress-SANS rule for this colloidal dispersion,

$$S(\boldsymbol{q}; Pe) = 1 + \sum_{l,m} B^{+}_{l,m}(q; Pe)(Y_{l,m}(\Omega_k) + (-1)^m Y_{l,-m}(\Omega_k)), \tag{3.1}$$

where the scalar coefficients $B^{+}_{l,m}(q; Pe)$ are determined from the scattering measurements as described below.

For reference, we present here the expressions derived in Wagner & Ackerson (1992) for the thermodynamic (equations (3.2)–(3.4)) and hydrodynamic (equations (3.5)–(3.7)) contributions to the total shear and normal stress responses. Both types of stress contributions are functions of the $B^{+}_{l,m}$ microstructure terms defined for a spherical harmonic expansion of the microstructure in reciprocal space and Pe (2.1), the dimensionless shear rate of deformation and ρ the particle number density:

$$\sigma^{T}(Pe) = -\frac{\rho}{\pi\sqrt{30\pi}} \int \theta^{*}(q) B^{+}_{2,1}(q; Pe) q^2 \, \mathrm{d}q, \tag{3.2}$$

$$\Psi_1^{T}(Pe) = \frac{\rho}{\pi\sqrt{30\pi}} \int \theta^{*}(q)(B^{+}_{2,2}(q; Pe) - \sqrt{6} B^{+}_{2,0}(q; Pe)) q^2 \, \mathrm{d}q, \tag{3.3}$$

$$\Psi_2^{T}(Pe) = \frac{\rho}{\pi\sqrt{30\pi}} \int \theta^{*}(q)(B^{+}_{2,2}(q; Pe) + \sqrt{6} B^{+}_{2,0}(q; Pe)) q^2 \, \mathrm{d}q, \tag{3.4}$$

$$\frac{\sigma^H(Pe)}{2\dot{\gamma}\eta_f} = 1 + \frac{5}{2}\phi(1+\phi) + 2.7\phi^2 + \frac{5}{2}\phi\sqrt{\pi}\int\left[B^+_{0,0}(q;Pe)\left(2\alpha(q)+\frac{4}{15}\zeta_0(q)\right) + B^+_{2,0}(q;Pe)\left(\frac{2}{3\sqrt{5}}\beta(q)+\frac{4\sqrt{2}}{15\sqrt{7}}\zeta_2(q)\right) + B^+_{2,2}(q;Pe)\left(\frac{2\sqrt{2}}{105}\zeta_2(q)+\sqrt{\frac{2}{15}}\beta(q)\right) + B^+_{4,0}(q;Pe)\left(\frac{-16}{105}\zeta_4(q)\right) + B^+_{4,2}(q;Pe)\left(\frac{4\sqrt{2}}{21\sqrt{5}}\zeta_4(q)\right)\right]q^2\,\mathrm{d}q \tag{3.5}$$

$$\frac{N_1^H(Pe)}{2\dot{\gamma}\eta_f} = -5\phi\sqrt{\pi} \times \int\left[B^+_{4,1}(q;Pe)\left(\frac{5\sqrt{2}+24\sqrt{5}}{105\sqrt{30}}\zeta_4(q)\right) + B^+_{4,3}(q;Pe)\left(\frac{1}{3\sqrt{35}}\zeta_4(q)\right)\right]q^2\,\mathrm{d}q, \tag{3.6}$$

$$\frac{N_2^H(Pe)}{2\dot{\gamma}\eta_f} = -5\phi\sqrt{\pi} \times \int\left[B^+_{2,1}(q;Pe)\left(\frac{2\sqrt{2}}{\sqrt{15}}\beta(q)+\frac{2\sqrt{2}}{7\sqrt{15}}\zeta_2(q)\right) + B^+_{4,1}(q;Pe)\left(\frac{5\sqrt{6}+24\sqrt{5}}{105\sqrt{30}}\zeta_4(q)\right) + B^+_{4,3}(q;Pe)\left(\frac{1}{3\sqrt{35}}\zeta_4(q)\right)\right]q^2\,\mathrm{d}q. \tag{3.7}$$

The stresses can also be expressed in terms of an expansion in real space; and the derivation for the hydrodynamic stresses is presented in appendix A. Comparison of the expressions in reciprocal space shown above with the results for real space in appendix A shows the same symmetries contributing to each stress component. This facilitates the direct comparison of structural anisotropy evident in scattering experiments with those evident in direct observation or simulations of the pair distribution function. (Note that (3.6) and (3.7) correct a typographical error in equation (62) of Wagner & Ackerson (1992).)

The spherical harmonic expansion of the 3D microstructure in reciprocal space, (3.1), is projected onto the three planes of flow measured during the flow- and rheo-SANS experiments to define the weighted functions $W_n(q,\ \dot{\gamma})$ (the full derivation of this expansion is presented in the supplementary data available at http://dx.doi.org/10.1017/jfm.2015.128 (Gurnon 2014)). These measurable functions

are defined for the velocity–velocity gradient (1–2) plane, where the neutron beam travels parallel to the 'vorticity' direction (hence the 'vorticity' superscript in (3.10)), the velocity–vorticity (1–3) plane, where the 'gradient' superscript is used in (3.11), and the velocity gradient–vorticity (2–3) plane, for which the neutron beam travels parallel to the velocity direction (here the 'velocity' superscript is used in (3.12)). Note that these are also functions of Pe through $B^{+}_{l,m}(q; Pe)$.

We define the weighted average functions $W_n(q, \dot{\gamma})$s for each plane. Operationally, to determine the $W_n(q, \dot{\gamma})$ values experimentally for each plane, the measured scattering during shear is divided by the equilibrium scattering (measured under quiescent conditions). In this way, we focus on the changes in the microstructure caused by shear. The analysis of the flow- or rheo-SANS experimental 2D scattering data proceeds by integrating over the azimuthal angle weighted by the functions $\cos(n\theta)$, where n is an integer (0, 2 or 4), or $\cos(\theta)\sin(\theta)$:

$$W_n(q, \dot{\gamma}) = \frac{1}{2\pi}\int_0^{2\pi} \cos(n\phi)\frac{I(q, \phi, \dot{\gamma})}{I(q, \dot{\gamma}=0)}\,\mathrm{d}(\phi), \quad n = 0, 2, 4, \ldots, \tag{3.8}$$

$$W_{21}(q, \dot{\gamma}) = \frac{1}{2\pi}\int_0^{2\pi} \cos(\phi)\sin(\phi)\frac{I(q, \phi, \dot{\gamma})}{I(q, \dot{\gamma}=0)}\,\mathrm{d}(\phi). \tag{3.9}$$

Inserting the spherical harmonic expansion for the structure factor identifies the contributions of specific symmetries of the structure to each weighted integral over the scattering patterns as

$$\begin{aligned} W_0^{vorticity}(q)S^{eq}(q) \;=\; & 1 + B^{+}_{0,0}(q)\left(\frac{1}{\sqrt{\pi}}\right) + B^{+}_{2,0}(q)\left(\frac{1}{4}\sqrt{\frac{5}{\pi}}\right) + B^{+}_{2,2}(q)\left(\frac{1}{4}\sqrt{\frac{15}{2\pi}}\right) \\ & + B^{+}_{4,0}(q)\left(\frac{27}{64\sqrt{\pi}}\right) + B^{+}_{4,2}(q)\left(\frac{9\sqrt{5}}{32\sqrt{2\pi}}\right) \\ & e + B^{+}_{4,4}(q)\left(\frac{9\sqrt{35}}{64\sqrt{2\pi}}\right) + \cdots \quad (l > 4), \end{aligned} \tag{3.10a}$$

$$\begin{aligned} W_2^{vorticity}(q)S^{eq}(q) \;=\; & B^{+}_{2,0}(q)\left(\frac{1}{4}\sqrt{\frac{5}{\pi}}\right) - B^{+}_{2,2}(q)\left(\frac{1}{8}\sqrt{\frac{15}{2\pi}}\right) + B^{+}_{4,0}(q)\left(\frac{60}{128\sqrt{\pi}}\right) \\ & + B^{+}_{4,2}(q)\left(\frac{3\sqrt{5}}{16\sqrt{2\pi}}\right) - B^{+}_{4,4}(q)\left(\frac{3\sqrt{35}}{32\sqrt{2\pi}}\right) + \cdots \quad (l > 4), \end{aligned} \tag{3.10b}$$

$$\begin{aligned} W_4^{vorticity}(q)S^{eq}(q) \;=\; & 2\left(B^{+}_{4,0}(q)\left(\frac{105}{64\sqrt{\pi}}\right) - B^{+}_{4,2}(q)\left(\frac{21\sqrt{5}}{16\sqrt{2\pi}}\right)\right. \\ & \left. + B^{+}_{4,4}(q)\left(\frac{3\sqrt{35}}{64\sqrt{2\pi}}\right)\right), \end{aligned} \tag{3.10c}$$

$$W_6^{vorticity}(q)S^{eq}(q) = 0, \tag{3.10d}$$

$$W_{21}^{vorticity}(q)S^{eq}(q) = \frac{1}{8}\left(B^{+}_{2,1}(q)\left(\sqrt{\frac{15}{2\pi}}\right) + B^{+}_{4,1}(q)\left(\frac{3\sqrt{5}}{8\sqrt{\pi}}\right)\right) + \cdots \quad (l > 4), \tag{3.10e}$$

$$W_0^{gradient}(q)S^{eq}(q) = 1 + B^+_{0,0}(q)\left(\frac{1}{\sqrt{\pi}}\right) - B^+_{2,0}(q)\left(\sqrt{\frac{5}{4\pi}}\right) + B^+_{4,0}(q)\left(\frac{9}{8\sqrt{\pi}}\right) + \cdots \quad (l > 4), \tag{3.11a}$$

$$W_2^{gradient}(q)S^{eq}(q) = B^+_{2,2}(q)\left(\sqrt{\frac{15}{8\pi}}\right) + B^+_{4,2}(q)\left(\frac{-3\sqrt{5}}{4\sqrt{2\pi}}\right) + \cdots \quad (l > 4), \tag{3.11b}$$

$$W_4^{gradient}(q)S^{eq}(q) = 4B^+_{4,4}(q)\left(\frac{3\sqrt{35}}{32\sqrt{2\pi}}\right) + \cdots \quad (l > 4), \tag{3.11c}$$

$$W_6^{gradient}(q)S^{eq}(q) = W_{12}^{gradient}(q)S^{eq}(q) = 0, \tag{3.11d}$$

$$W_0^{velocity}(q)S^{eq}(q) = 1 + B^+_{0,0}(q)\left(\frac{1}{\sqrt{\pi}}\right) + B^+_{2,0}(q)\left(\frac{1}{4}\sqrt{\frac{5}{\pi}}\right) + B^+_{2,2}(q)\left(\frac{1}{4}\sqrt{\frac{15}{2\pi}}\right) + B^+_{4,0}(q)\left(\frac{27}{64\sqrt{\pi}}\right) - B^+_{4,2}(q)\left(\frac{15\sqrt{5}}{32\sqrt{2\pi}}\right) - B^+_{4,4}(q)\left(\frac{9\sqrt{35}}{64\sqrt{2\pi}}\right) + \cdots \quad (l > 4), \tag{3.12a}$$

$$W_2^{velocity}(q)S^{eq}(q) = \frac{1}{2}\left(B^+_{2,0}(q)\left(\frac{3}{4}\sqrt{\frac{5}{\pi}}\right) - B^+_{2,2}(q)\left(\frac{1}{4}\sqrt{\frac{15}{2\pi}}\right) - B^+_{4,0}(q)\left(\frac{60}{64\sqrt{\pi}}\right) - B^+_{4,2}(q)\left(\frac{6\sqrt{5}}{32\sqrt{2\pi}}\right) + B^+_{4,4}(q)\left(\frac{12\sqrt{35}}{64\sqrt{2\pi}}\right)\right) + \cdots \quad (l > 4), \tag{3.12b}$$

$$W_4^{velocity}(q)S^{eq}(q) = 2\left(-B^+_{4,0}(q)\left(\frac{105}{64\sqrt{\pi}}\right) + B^+_{4,2}(q)\left(\frac{21\sqrt{5}}{64\sqrt{2\pi}}\right) - B^+_{4,4}(q)\left(\frac{3\sqrt{35}}{64\sqrt{2\pi}}\right)\right) + \cdots \quad (l > 4), \tag{3.12c}$$

$$W_6^{velocity}(q)S^{eq}(q) = W_{12}^{velocity}(q)S^{eq}(q) = 0. \tag{3.12d}$$

These three sets of equations relate quantifiable functions obtainable from the rheo- and flow-SANS measurements to the $B^+_{l,m}$ microstructure terms. In this work we use the experimental results from rheo- and flow-SANS experiments to define the $W_n(q, \dot{\gamma})$ functions in order to gain a quantitative measure for the microstructure that is, within a constant, equal to the stress. As is discussed here, the proportionality constants $C^{\sigma,T}$, $C_0^{\sigma,H}$, $C_4^{\sigma,H}$, $C^{N1,H}$ and $C^{N1,T}$ are scalars defined once for a particular colloidal dispersion under steady shear and then employed to predict those corresponding stresses under other steady and dynamic shear conditions.

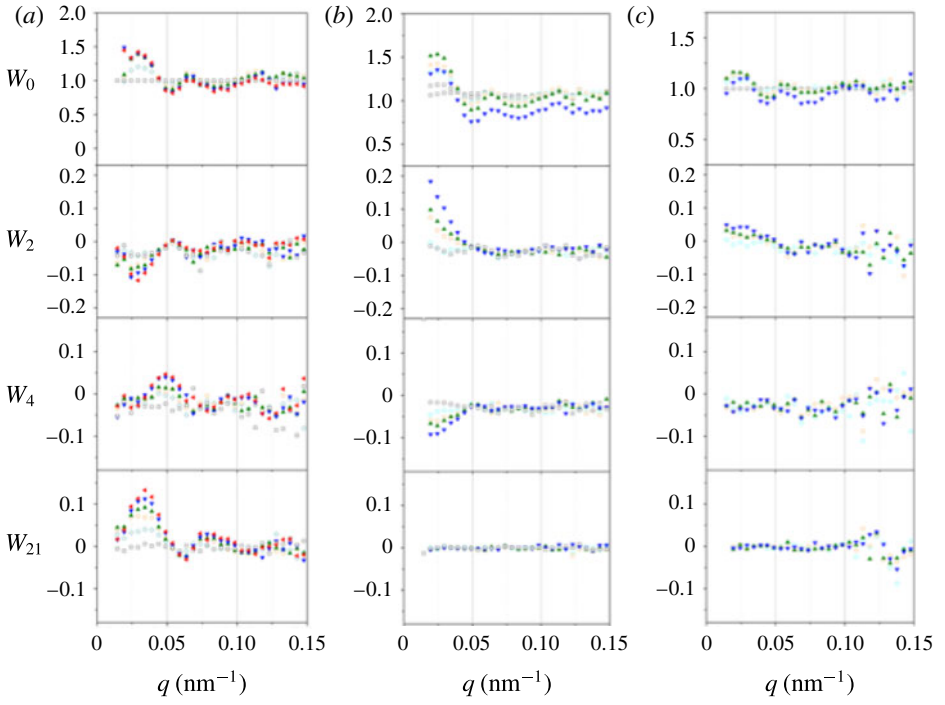

FIGURE 6. (Colour online) Plots of W_n as a function of q (nm^{-1}) as defined in (3.8) and (3.9), where $\dot{\gamma} = 0$ s^{-1} (□), 12 s^{-1} (◇), 62 s^{-1} (○), 127 s^{-1} (▲), 627 s^{-1} (▼) and 1255 s^{-1} (◀). Panels correspond to scattering experiments performed in the (*a*) 1–2, (*b*) 1–3 and (*c*) 2–3 planes.

Figure 6 shows the $W_n(q, \dot{\gamma})$ as defined from (3.8) and (3.9) for each shear rate and plane measured during flow- and rheo-SANS experiments. It is best to discuss and understand the rich shear-induced microstructure presented in this way because significant differences in the microstructure are detectable at different scattering lengths and shear rates. To begin with, the W_0 in all three planes is the intensity normalized by the zero-shear intensity with no weighting applied to the annular integrated scattering. This function provides a quantitative measure of the number of nearest neighbours regardless of angular position (see figure 7*a*,*e*). In figure 6 W_0 shows clear increases in the scattered intensity. As the functions are normalized by the equilibrium values, this increase for low q values and decrease for q values above the primary peak position correspond to a shift to lower q of the primary peak. The increase in magnitude is indicative of a greater number of neighbouring particles probed, whereas a shift in the peak to lower q suggests that larger length-scale structures are observed, such as those reported by Kalman & Wagner (2009). In the 1–2 plane of shear, the intensity saturates for $\dot{\gamma} > 62$ s^{-1}, suggesting that increasing shear rates do not lead to more nearest neighbours in this regime. This is important for understanding why the first-order microstructure contribution to the stress is not adequate for predicting the shear thickening response, as noted previously (Maranzano & Wagner 2002; Kalman 2010). In the other two planes, a decrease in the total intensity is observed for $\dot{\gamma} > 627$ s^{-1}. At these higher shear rates, the sample integrity is compromised, and air bubbles are introduced in the cup-and-bob Couette

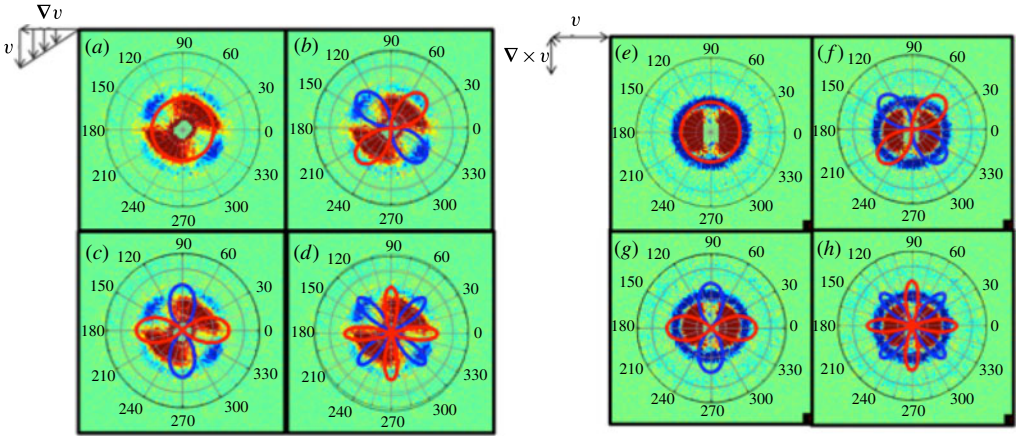

FIGURE 7. Scattering results overlaid with the weighting functions in two planes: (*a*) 1–2 flow-SANS and (*b*) 1–3 rheo-SANS. Weighting functions are used in (3.8), $\cos(n\phi_{21})$, where $n = 0$, 2 and 4 (for *a*,*e*, *c*,*g* and *d*,*h* respectively) and in (3.9), $\cos(\phi_{21})\sin(\phi_{21})$, for *b*,*f*. The function is either red or blue, indicating a positive or negative value of the function, respectively. Similarly, the SANS scattering patterns are subtracted patterns from a quiescent scattering pattern, and therefore the warmer colours indicate more scattering events while the cooler colours indicate fewer scattering events during shear than those that occur at equilibrium.

geometry during radial and tangential rheo-SANS experiments such that the intensity in the scattering decreases. Transmission measurements confirm this instability, and no further analysis will be performed in these conditions. Note that no such problems are observed for the 1–2 shear cell at these shear rates, as it is sealed and air bubbles are not observed, again confirmed by transmission measurements.

The W_2 weighting functions reported in figure 6 give a quantitative measure for any changes in the twofold symmetry structure that might exist during flow in each of the three planes, where the specific microstructural symmetries involved depend on the plane of measurement (see (3.10)–(3.12)). Figure 7(*c*) shows that the $\cos(2\phi)$ weighting function is positive in the lobes along the 0° and 180° detector angles, whereas it is negative at detector angles of 90° and 270°. Since more structure is observed along the $\phi_{21} = 90°$ and 270° detector angles in the 1–2 plane of shear, the function becomes more negative with increasing shear rate. Precisely the opposite is the case for the 1–3 plane (figure 7*g*), where the W_2 function increases to more positive values with increasing shear rate, indicative of more structure along the $\phi_{13} = 0°$ and 180° detector angles for the velocity–vorticity plane. In the 1–3 plane, the q range accessible is not small enough to capture the peak in the intensity, indicating that larger structures (consisting of more than a particle and its nearest neighbour) form in the velocity–vorticity plane. This observation is consistent with observations made based on the 2D scattering patterns discussed in the previous sections, which indicate that particles have a propensity to associate along the vorticity direction. The trend in the velocity gradient–vorticity (2–3) plane is similar to that in the 1–3 plane; however, the magnitude of the changes is less.

The fourfold symmetry microstructure changes are defined using the W_4 weighting function (figure 7*d*). In the velocity–velocity gradient plane of shear, the fourfold symmetry increases with increasing shear rate at a q larger than observed for the

changes in the twofold symmetry (figure 6). The shift to larger q is indicative of the fourfold symmetric microstructure occurring at length scales of the order of the nearest-neighbour peak in the structure factor ($q_{peak} = 0.042$–0.064 nm^{-1}) in figure 2(*a*). Interestingly, this shift in q is not observed in either of the other planes of shear. The fourfold symmetry in the 1–2 plane is caused by increased intensity along the velocity and velocity gradient directions (figure 7*d*). At such a high concentration of suspended particles ($\phi_{eff} = 0.465$), it is possible that this fourfold symmetry is the result of packing effects made more apparent by the high shear rates, which induce hydrocluster formation in the shear thickening regime. The onset of fourfold symmetry in the microstructure of concentrated suspensions has been observed in simulations by Nazockdast & Morris (2013). Their calculations show a propensity to find fourfold coordination of nearest neighbours at higher (>30 %) packing fractions. However, for this symmetry to become apparent in our scattering measurements, it will need to be oriented by the flow. Clearly, this fourfold symmetry becomes apparent at high shear rates where shear thickening is evident. There are only small changes in W_4 in the 1–3 plane of shear. If anything, the function trends to more negative values with increasing rates. Figure 7(*h*) shows that this is the result of the $\cos(4\phi_{13})$ function's constructive weighting of the increasing intensity in the vorticity direction of shear, thereby resulting in increases in fourfold symmetry opposite in sign to those twofold microstructure changes defined by W_2. There are no fourfold symmetry microstructures measured in the 2–3 plane.

The higher-order two- and fourfold symmetric scattering functions show measurable changes during shear flow. However, care needs to be taken in defining priority to the contributions bearing in mind the initial weighting functions used to assess the microstructure's symmetry. In fact, based on the definitions for the two- and fourfold symmetry, these functions could be different measures of the same structural features. The increases in two- and fourfold weighted scattering functions are not independent given the weighting functions used to assess the microstructure in the 1–2 plane (figure 7*c*,*d*). As changes in fourth-order harmonics can also appear in the definition of $W_2(\dot{\gamma})$, we focus our attention on the readily apparent increases in $W_4(\dot{\gamma})$.

Specifically, the fourfold symmetric functions increase in intensity in the velocity and velocity gradient directions observed in the 2D scattering patterns, which is a symmetry that also contributes to twofold symmetry increases, given the definitions of $W_2(\dot{\gamma})$ and $W_4(\dot{\gamma})$. Therefore, it is most important to include the fourfold symmetry microstructure in the velocity–velocity gradient plane of shear. An analogous argument can be made for the velocity–vorticity (1–3) plane; figure 7(*g*,*h*) shows these microstructures in the velocity–vorticity plane and velocity–velocity gradient planes. It is clear that the microstructure with true twofold symmetry could also contribute to W_4, given the definition for the weighting function applied. However, by inspecting the 2D scattering pattern, we find it is most important to include the shear-induced twofold symmetry in the 1–3 plane.

A rigorous evaluation of the stresses from the SANS data requires evaluating $W_n(q, \dot{\gamma})$ for all q, but it is not experimentally possible to measure to infinite q. Thus, following previous work, we choose to define a q range for which the maximum microstructure changes due to shear are observed during the experiment (Maranzano & Wagner 2002). Figure 6 indicates the location of the largest changes in weighted intensity as a function of scattering vector, $\boldsymbol{q}$. Table 2 gives the q_{min} and q_{max} for which the integral defined in (3.13) is taken for each of the different weighting functions in each of the planes according to

$$\overline{W_n(\dot{\gamma})} = \frac{1}{\Delta(aq)} \int_{aq_{min}}^{aq_{max}} W_n(q, \dot{\gamma})(aq)^2 \, \mathrm{d}(aq). \tag{3.13}$$

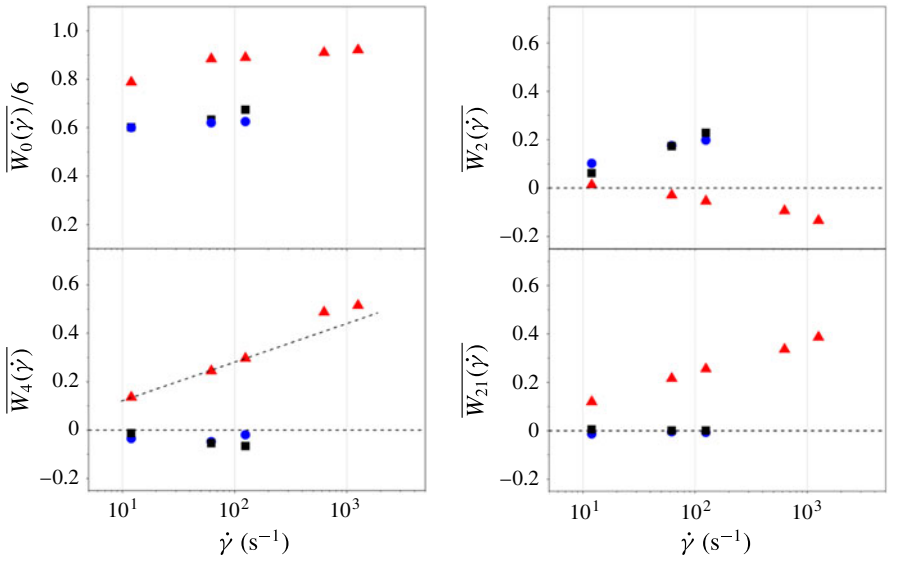

FIGURE 8. (Colour online) For the 1–2 (▲), 1–3 (■) and 2–3 (●) planes, the $\overline{W_n(\dot\gamma)}$ values as defined in (3.13), where q_{min} and q_{max} are defined in table 2. The $\overline{W_n(\dot\gamma)}$ values have been shifted such that $\overline{W_n(\dot\gamma = 0)} = 0$ and a trend line has been added for $\overline{W_4(\dot\gamma)}$ for clarity.

Plane interrogated	Weighting function	q_{min}–q_{max} (nm^{-1})	Real space ($\sim 2\pi/\boldsymbol{q}$) (nm)
1–2	$\cos(0\theta)$	0.0194–0.0539	∼116–323
	$\cos(2\theta)$	0.0194–0.049	∼116–323
	$\cos(4\theta)$	0.0342–0.0638	∼99–183
	$\cos(\theta)\sin(\theta)$	0.0194–0.0539	∼116–323
1–3	$\cos(0\theta)$	0.0194–0.0342	∼183–324
	$\cos(2\theta)$	0.0194–0.049	∼128–324
	$\cos(4\theta)$	0.0194–0.049	∼128–324
	$\cos(\theta)\sin(\theta)$	0.0194–0.049	∼128–324
2–3	$\cos(0\theta)$	0.0194–0.0391	∼160–324
	$\cos(2\theta)$	0.0194–0.049	∼128–324
	$\cos(4\theta)$	0.0194–0.049	∼128–324
	$\cos(\theta)\sin(\theta)$	0.0194–0.049	∼128–324

TABLE 2. The q_{min} and q_{max} values used to define $\overline{W_n(\dot\gamma)}$.

The $\overline{W_n(\dot\gamma)}$ are now only a function of shear rate and define the weighting functions integrated over the scattering vector ($\boldsymbol{q}$ nm^{-1}) in table 2, which is always normalized by the particle radius ($a = 61.1$ nm). Figure 8 reports those $\overline{W_n(\dot\gamma)}$ for the 1–2, 1–3 and 2–3 planes.

Inspection of figure 8 shows that both $\overline{W_2^{vorticity}}(\dot\gamma)$ and $\overline{W_4^{vorticity}}(\dot\gamma)$ vary substantially with shear rate and are of the same order (but opposite in sign) and, therefore, could both potentially be the next-order contribution to the hydrodynamic stress. The

relationship between these two contributions is entrenched in the expressions given in (3.4), such that it is not immediately obvious which contribution should be used to define the additional hydrodynamic stress responses in the shear thickening regime. Furthermore, the $\overline{W_2^{vorticity}}(\dot{\gamma})$ decreases with increasing shear rate while the $\overline{W_4^{vorticity}}(\dot{\gamma})$ shows a significant increase in values between $\dot{\gamma} = 125$ and 627 s^{-1} (a trend line is provided to illustrate this) corresponding to a transition from the shear thinning to the shear thickening regime. Since there is a significant change in the stress contribution for the shear thickening regime ($\dot{\gamma} > 295$ s^{-1}, $Pe > 12.3$), we choose to associate the $\overline{W_4^{vorticity}}(\dot{\gamma})$ with the additional hydrodynamic microstructure contributions to the stress.

The W_{21} weighting function is clearly only measured in the velocity–velocity gradient plane as is expected given (3.10)–(3.12). These measurements show increases in intensity at a constant q range clearly indicative of more structure forming with increasing shear rate (figure 8). This type of symmetry is caused by particles being forced together along the compression axis of flow as the sample is sheared. Neither the radial or tangential planes measure the microstructure in the shear plane where one can interrogate the compression axis, and therefore this weighted scattering function is expected to be, and is, exactly zero in the other two planes for all shear conditions.

In the following section, the $\overline{W_n^{vorticity}}(\dot{\gamma})$ given in figure 8 is used to define the stress-SANS rule such that the microstructure stress contribution is comparable to the shear stress response measured during a rheometry experiment. Figure 8 clearly shows that there are contributions from higher-order microstructures ($W_2(\dot{\gamma})$ and $W_4(\dot{\gamma})$) in all of the planes of equal magnitude to those microstructures that contribute to the thermodynamic stress during steady shear. Most notable are those measurements in the 1–2 plane of shear for the $\overline{W_2^{vorticity}}(\dot{\gamma})$ and $\overline{W_4^{vorticity}}(\dot{\gamma})$ terms. As was discussed previously, there is difficulty in deconvoluting these two types of symmetries into separate contributions to the hydrodynamic stress. As will be shown in the next section, it is sufficient to include those fourth-order harmonic microstructure terms to reconcile the hydrodynamic stresses in the shear thickening regime.

All three planes of shear flow are necessary for fully determining the 3D microstructure and all contributions to the stress tensor. However, with some simplifying assumptions, a reduced set of measurements can be used to obtain the stresses from the harmonic expansion of the microstructure. Importantly, in this work, the new scattering measurements in the velocity–velocity gradient (1–2) plane of shear (first column of figure 6) will be used to define the majority of the structure harmonics necessary for defining the stress-SANS rule. Previous research (Foss & Brady 2000; Maranzano 2001; Kalman 2010) has shown that the only plane of observation capable of defining the thermodynamic contribution to the shear stress is the 1–2 plane. Note that the dominant hydrodynamic contribution can be defined in the plane of shear as well. However, defining the thermodynamic contribution to the normal stress differences requires measurements in the 1–3 plane, as will be shown. The corresponding stress-SANS rules are defined in the following subsections.

3.2.1. *Stress-SANS rule: thermodynamic shear stress*

The thermodynamic stress contribution is formally exact and the shear stress is shown to be proportional to only those contributions arising from the $B_{2,1}^{+}$ symmetry term of the microstructure (3.2). Equation (3.10) is the only equation that includes the $B_{2,1}^{+}$ microstructure term in the expansion for the microstructure in any plane measured

Coefficient	Value	Units
$C^{\sigma,T}$	22	Pa
$C_0^{\sigma,H}$	0.063	—
$C_4^{\sigma,H}$	4.6	—
$C^{N1,H}$	−5.2	—
$C^{N1,T}$	18	Pa

TABLE 3. Summary of coefficients for stress-SANS rule.

during a rheo- or flow-SANS experiment. Therefore $\overline{W_{21}^{vorticity}}$ measured by flow-SANS experiments made in the 1–2 plane of shear defines the thermodynamic stress contribution to the total stress response measured during a rheometry experiment.

The $\overline{W_{21}^{vorticity}}$ microstructure contribution is proportional to the thermodynamic stress contribution. At the lowest shear rates, the thermodynamic contribution to the total stress is largest; therefore, the lowest shear rate for which the microstructure has been measured is chosen to determine the thermodynamic constant. The proportionality constant will be defined for the $\dot{\gamma} = 12\ \mathrm{s}^{-1}$ condition and hereafter will be applied to each microstructure measured to determine the thermodynamic stress contribution from the microstructure at any other shear rate. The thermodynamic stress constant ($C^{\sigma,T}$) is equal to

$$C^{\sigma,T} = \frac{\sigma_r(\dot{\gamma}) - \sigma_{fit}(\dot{\gamma})}{\overline{W_{21}^{vorticity}}(\dot{\gamma})}, \tag{3.14}$$

where σ_r is the stress measured during a rheometry measurement and σ_{fit} is the hydrodynamic stress extrapolated from a linear fit of the stress at shear rates close to the critical shear rate for shear thickening ($\dot{\gamma}_c = 295\ \mathrm{s}^{-1}$, $Pe = 12.3$) given in figure 9(*a*). This is justified because the stress response at shear rates greater than or equal to the critical shear rate for an STF are largely hydrodynamic in nature (Bender & Wagner 1996; Banchio & Brady 2003). Figure 9(*b*) confirms this, where the high shear viscosity ($\eta_{r,\infty}$) prior to shear thickening is quantitatively consistent with that for hard spheres. In addition, the hydrodynamic microstructure's contribution to the stress is proportional to the shear rate (see (3.5)). Therefore, a good approximation for the hydrodynamic stress at the lowest shear rates is the extrapolation of the fit to high shear rates. A similar procedure was used in previous work analysing the other planes of flow (Maranzano & Wagner 2002). The coefficient is defined using the microstructure measured at the $\dot{\gamma} = 12\ \mathrm{s}^{-1}$ condition and the fit shown in figure 9. For this suspension, $C^{\sigma,T} = 22$ Pa and is also reported in table 3.

Now that the thermodynamic coefficient is defined, the thermodynamic stress contribution at any shear rate $\sigma^T(\dot{\gamma})$ is defined given $\overline{W_{21}^{vorticity}}$ from a flow-SANS microstructure measurement made in the velocity–velocity gradient plane of shear and the following expression:

$$\sigma^T(\dot{\gamma}) = C^{\sigma,T}\left(\overline{W_{21}^{vorticity}}(\dot{\gamma})\right). \tag{3.15}$$

Figure 9 shows the thermodynamic stress contribution calculated from the stress-SANS rule as a function of shear rate and *Pe*. Clearly, the thermodynamic stress is always increasing with *Pe*. However, as expected, this stress contribution grows

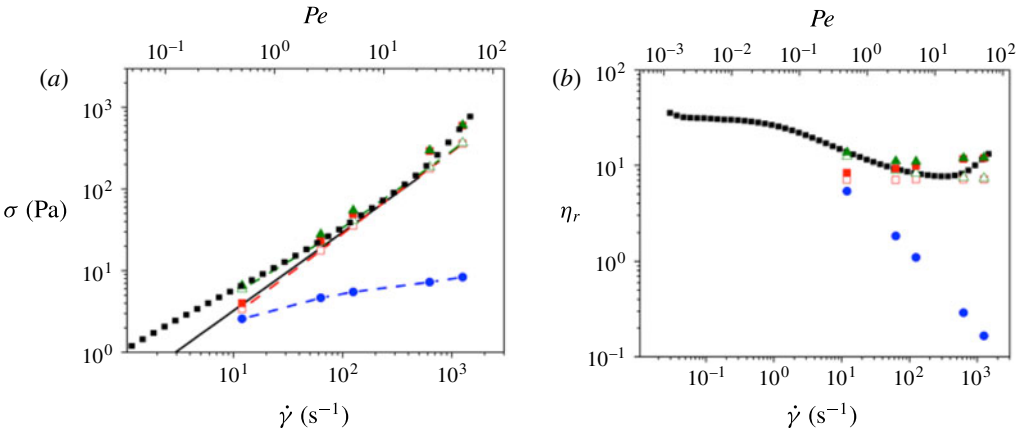

FIGURE 9. (Colour online) (*a*) Stress and (*b*) relative viscosity $\eta_r = \eta(T)/\eta_f(T)$ as functions of $\dot{\gamma}$ and *Pe*. Symbols: rheometry results, black filled square; stress-SANS rule thermodynamic stress, filled circle (blue online); first-order hydrodynamic stress, open square (red online); and total stress, open triangle (green online). Also included are: stress-SANS rule higher-order hydrodynamic contributions for hydrodynamic stress, filled square (red online); and total stress, filled triangle (green online). The line (black) is fitted to the stress responses for $\dot{\gamma} = 199.6$–500.1 s^{-1} around the critical shear rate $\dot{\gamma} = 295$ s^{-1}.

more slowly at higher $\dot{\gamma}$ as a result of saturation of the microstructure deformation (Wagner *et al.* 1988; Bender & Wagner 1995). As the thermodynamic stress is directly proportional to the microstructure deformation, and this deformation cannot continue to increase linearly with the shear rate for even modest *Pe*, it ultimately increases as a function of shear rate with power-law exponent of $\sim 1/2$. The thermodynamic stress contribution is strongly shear thinning, and this change is largely responsible for the shear thinning rheology observed in figure 9(*b*).

3.2.2. *Stress-SANS rule: hydrodynamic shear stress*

In contrast to the thermodynamic stress, the hydrodynamic stress in (3.5) includes many terms from the structure factor expansion including up to fourth-order terms ($B^+_{0,0}$, $B^+_{2,0}$, $B^+_{2,2}$, $B^+_{4,0}$ and $B^+_{4,2}$). The definition of the $W_0^{vorticity}$ weighting function defined in (3.10) includes all of these microstructure contributions. As expected from previous experimental measures by Maranzano & Wagner (2002), the $\overline{W_0^{vorticity}}(\dot{\gamma})$ term measured from the microstructure is an order of magnitude larger than any of the other microstructure contributions shown in figure 8. The first-order contribution to the hydrodynamic stress is proportional to those microstructure changes captured in $\overline{W_0^{vorticity}}(\dot{\gamma})$. Therefore, the coefficient for the first-order hydrodynamic stress contribution ($C_0^{\sigma,H}$) is defined by

$$C_0^{\sigma,H} = \frac{(2\eta_f\dot{\gamma})^{-1}[\sigma_r(\dot{\gamma}) - \sigma^T(\dot{\gamma})] - [1 + \frac{5}{2}\phi(1+\phi) + 2.7\phi^2]}{\overline{W_0^{vorticity}}(\dot{\gamma})}. \tag{3.16}$$

We anticipate that the shear thickening regime will have additional higher-order microstructure contributions to the total stress. However, this first-order contribution is expected to accurately predict the hydrodynamic stress contributions in the shear

thinning regime. The hydrodynamic stress contribution is defined for the SANS condition measured at the largest shear rate in the shear thinning regime (and closest to the critical shear rate for shear thickening). For the measurements made here, the shear condition $\dot{\gamma} = 125\ \mathrm{s}^{-1}$ gives a constant coefficient for the hydrodynamic stress contribution reported in table 3 and is $C_0^{\sigma,H} = 0.063$.

Now that the first-order hydrodynamic stress-SANS coefficient ($C_0^{\sigma,H}$) is defined, it is possible to predict the first-order hydrodynamic stress contribution $\sigma_0^H(\dot{\gamma})$ given a measure of $\overline{W_0^{vorticity}}(\dot{\gamma})$ from the microstructure at any shear condition with the expression:

$$\frac{\sigma_0^H(\dot{\gamma})}{2\eta_f\dot{\gamma}} = C_0^{\sigma,H}\left(\overline{W_0^{vorticity}}(\dot{\gamma})\right). \tag{3.17}$$

Figure 9 shows the first-order hydrodynamic stress contribution as a function of shear rate and Pe. For all Pe probed, the hydrodynamic stress is always larger than the thermodynamic stress response, which is anticipated for $Pe \sim O(1)$ or larger. In addition, the sum of the hydrodynamic and thermodynamic stress responses in the shear thinning regime $Pe < 12.3$ agree well with those stresses measured in a bulk rheology experiment. However, for those measurements made in the shear thickening regime, the microstructure's total stress defined using only the first-order contribution from the hydrodynamic stress and the thermodynamic stress is significantly lower than those measured responses from a rheometry experiment.

It is with this discrepancy in mind that we look at higher-order microstructure contributions to the hydrodynamic stress such that the shear thickening response will also be well predicted from the microstructural changes experimentally measured during shear thickening. Therefore, the constant for the higher-order hydrodynamic stress contribution is defined here as

$$C_4^{\sigma,H} = \frac{(2\eta_f\dot{\gamma})^{-1}[\sigma_r(\dot{\gamma}) - \sigma^T(\dot{\gamma}) - \sigma_0^H(\dot{\gamma})] - [1 + \frac{5}{2}\phi(1+\phi) + 2.7\phi^2]}{\overline{W_4^{vorticity}}(\dot{\gamma})}, \tag{3.18}$$

where the higher-order coefficient for fourfold symmetry is defined by the microstructure measured for the shear thickening condition at $\dot{\gamma} = 1258\ \mathrm{s}^{-1}$. The coefficient is therefore $C_4^{\sigma,H} = 4.6$ (also reported in table 3). Analogous to the expression given in (3.17), for all conditions the higher-order hydrodynamic stress contribution is calculated from

$$\frac{\sigma_4^H(\dot{\gamma})}{2\eta_f\dot{\gamma}} = C_4^{\sigma,H}\left(\overline{W_4^{vorticity}}(\dot{\gamma})\right). \tag{3.19}$$

The total stress is then defined as the sum of the stress contributions from the thermodynamic, first-order hydrodynamic and higher-order hydrodynamic stresses from fourfold microstructure symmetry defined in (3.15), (3.17) and (3.19) and given here as

$$\sigma^{total}(\dot{\gamma}) = \sigma^T(\dot{\gamma}) + 2\eta_f\dot{\gamma}[1 + \tfrac{5}{2}\phi(1+\phi) + 2.7\phi^2] + \sigma_0^H(\dot{\gamma}) + \sigma_4^H(\dot{\gamma}). \tag{3.20}$$

Figure 9 shows the final results, which include the fourfold symmetry hydrodynamic microstructure contribution to the stress in comparison to the rheometry measured stress. By including the higher-order hydrodynamic stress contribution contained in this structure component, we can largely reconcile the stress response in the shear thickening regime. However, the stresses in the shear thinning regime are slightly

overpredicted, having included an additional hydrodynamic microstructure contribution. Including the fourfold symmetric structure contributions in the stress-optic law for the hydrodynamics semiquantitatively accounts for the increased dissipation in the shear thickening state.

Finally, figure 9(*b*) presents the relative viscosity $\eta_r = \eta(T)/\eta_f(T)$ as a function of *Pe* as defined from rheometry measurements and the stress-SANS rule, for which the zero-shear viscosity $\eta_{0,r} = 25.4$ and the high-frequency viscosity $\eta'_{\infty,r} = 5.90$ are defined according to theory for a hard-sphere suspension having an effective volume fraction of $\phi_{eff} = 0.465$. The significant decrease in thermodynamic contribution to the viscosity is expected given the relatively small thermodynamic stress response measured at high *Pe*, shown in figure 9. The hydrodynamic stress response including the first- and fourth-order contributions tends towards the known limit of $\eta'_{\infty,r} = 5.90$ at low shear rates, as expected, given that for $Pe > 0$ the hydrodynamic viscosity should be greater than the high-frequency viscosity (Russel *et al.* 2013). In addition, the thermodynamic viscosity contribution decreases with increasing *Pe*, while the hydrodynamic contributions increase. These experimental results are qualitatively consistent with those Stokesian dynamics simulation results reported by Banchio & Brady (2003). Importantly, including contributions from fourth-order terms in the hydrodynamic contribution to the shear stress reconciles in part the quantitative discrepancies observed in the shear thickening regime.

3.2.3. *Stress-SANS rule: hydrodynamic normal stresses*

In addition to the shear stresses, the expressions in (3.3), (3.4), (3.6) and (3.7) also predict the first and second normal stress differences (N_1 and N_2). According to (3.6) only fourth-order microstructure symmetries $B^+_{4,1}$ and $B^+_{4,3}$ contribute to the hydrodynamic first normal stress. The thermodynamic normal stress is positive for suspensions, and so the measurement of a large negative first normal stress difference in the shear thickened state as shown in figure 1 necessitates that there are significant fourth-order symmetries in the microstructure. The microstructural symmetry is not independently isolated but appears in the term $\overline{W_{21}^{vorticity}}(\dot\gamma)$, which also includes the second-order term $B^+_{4,1}$. Although we cannot isolate these fourth-order symmetries independently, we know they exist as the first normal stress difference becomes large and negative, indicating a significant hydrodynamic contribution. Therefore, the first normal stress due to hydrodynamic interactions is given in (3.6) and is proportional to those changes measured by $\overline{W_{21}^{vorticity}}(\dot\gamma)$. Therefore the coefficient for the first normal stress difference is

$$C^{N1,H} = \frac{N_{1,r}(\dot\gamma)}{2\eta_f\dot\gamma\,\overline{W_{21}^{vorticity}}(\dot\gamma)}, \tag{3.21}$$

and defined for the microstructure condition measured at the $\dot\gamma = 627\ \mathrm{s}^{-1}$ shear rate condition. The coefficient for the first normal stress is given in table 3 ($C^{N1,H} = -5.2$). The coefficient is used to predict the first normal stress for all other conditions using the $\overline{W_{21}^{vorticity}}(\dot\gamma)$ microstructure measured during a flow-SANS experiment and the expression given here:

$$\frac{N_1^H(\dot\gamma)}{2\eta_f\dot\gamma} = C^{N1,H}\big(\overline{W_{21}^{vorticity}}(\dot\gamma)\big). \tag{3.22}$$

Figure 10 shows a comparison between the normal stress measured during a rheometry experiment and the stress predicted using the stress-SANS rule defined in (3.22). As

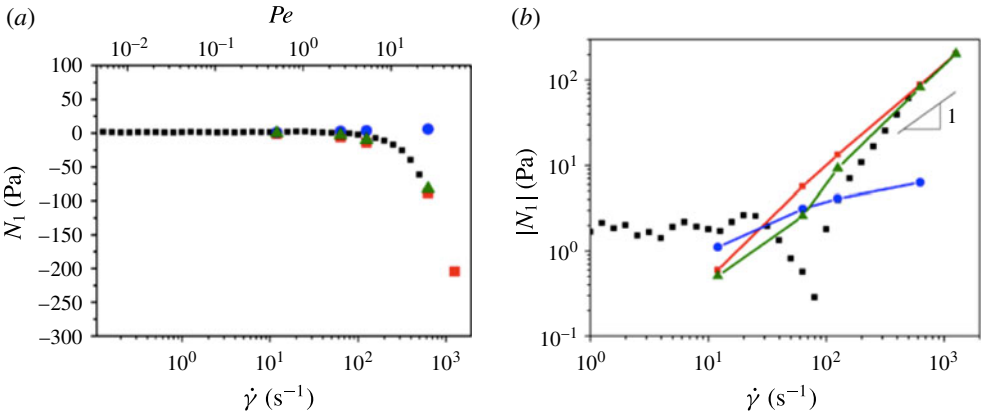

FIGURE 10. (Colour online) (*a*) Plot of the N_1 stress as a function of $\dot{\gamma}$ and Pe for steady shear rheometry measurements (black filled square) and defined by the stress-SANS rule for the hydrodynamic contribution (grey filled square; red online), thermodynamic contribution (filled circle; blue online) and the total (filled triangle; green online). Also reported in table 4. (*b*) The absolute value of the first normal stress and corresponding hydrodynamic, thermodynamic and total stress contributions defined by stress-SANS rules.

the normal stress difference is normalized upon loading a sample, the first normal stress should be exactly 0 Pa for quiescent conditions. Stokesian dynamics simulations predict the hydrodynamic contribution to the first normal stress to be increasingly negative and, in the limit of large Pe, to increase as Pe^{-1} as the suspension shear thickens (Foss & Brady 2000). Indeed, the largest normal stress effect measured for these particular rheometry measurements is the large negative values for the normal stress at high shear rates in the shear thickening regime. The hydrodynamic contribution to the normal stress should always be negative, as observed for these shear rates using the stress-SANS rule.

According to Stokesian dynamic simulations by Foss & Brady (2000) and Banchio & Brady (2003), the thermodynamic contribution to N_1 decreases with increasing Pe for $Pe > 1$. Therefore, it is not surprising that excellent agreement is observed between the hydrodynamic contribution to the first normal stress difference and the normal stress measured during a rheometry experiment at high shear rates. In a rheometry measurement, the shear and normal stresses are measurements made simultaneously during steady shear but are independent from one another. As has been discussed in previous work by Kalman (2010), the remarkable agreement observed in figure 10 also provides confidence in the SANS 1–2 shear flow measurements that the $B^{+}_{2,1}$ microstructure term is properly measured, isolated and analysed using $\overline{W_{21}^{vorticity}}(\dot{\gamma})$. This term accurately predicts the thermodynamic contribution to the shear stress and the hydrodynamic contribution to the first normal stress difference (defined in (3.2) and (3.6)).

3.2.4. *Stress-SANS rule: thermodynamic normal stresses*

The thermodynamic contribution to the first normal stress is defined by (3.3), where only the $B^{+}_{2,0}$ and $B^{+}_{2,2}$ microstructure terms are required to define N_1. Given the spherical harmonic expansion in reciprocal space, the $B^{+}_{2,2}$ and $B^{+}_{4,2}$ microstructure terms define the $\overline{W_2^{gradient}}(\dot{\gamma})$ (3.11) measured in the 1–3 plane during a rheo-SANS

Pe	N_1^H (Pa)	N_1^T (Pa)	N_1 (Pa)
0.50	−0.60	1.1	0.50
2.63	−5.70	3.12	−2.58
5.23	−13.4	4.13	−9.27
26.22	−88.4	6.33	−82.0
52.6	−204		

TABLE 4. Summary of first normal stress contributions using the stress-SANS rule.

experiment. The coefficient for the first normal stress difference is defined for the lowest shear rate for which we expect the largest contribution to the first normal stress difference from thermodynamic stresses where

$$C^{N1,T} = \frac{N_{1,r}(\dot{\gamma}) - N_1^H(\dot{\gamma})}{\overline{W_2^{gradient}(\dot{\gamma})}}. \tag{3.23}$$

The thermodynamic coefficient for the first normal stress is defined for the microstructure condition measured at the $\dot{\gamma} = 12\ \mathrm{s}^{-1}$ condition, from which we take the difference between the measured N_1 from a rheometry experiment and the hydrodynamic stress contribution predicted by (3.22). The coefficient for the first normal stress is given in table 3 ($C^{N1,T} = 18$ Pa). Not surprisingly, this coefficient is close in value to $C^{\sigma,T} = 22$ used to predict the thermodynamic contribution to the shear stresses. The coefficient is used to predict the first normal stress for all other conditions using the $\overline{W_2^{gradient}}(\dot{\gamma})$ microstructure measured during a flow-SANS experiment and the expression given here:

$$N_1^T(\dot{\gamma}) = C^{N1,T}\left(\overline{W_2^{gradient}}(\dot{\gamma})\right). \tag{3.24}$$

Figure 10 and table 4 report those predictions for the thermodynamic contribution to the first normal stress according to (3.24) and the sum of the thermodynamic and hydrodynamic normal stresses. Note that the thermodynamic and hydrodynamic normal stress contributions are opposite in sign. This is in good qualitative agreement with theory using the Smoluchowski equation for a pair of Brownian hard-sphere particles having hydrodynamic interactions as reported by Bergenholtz *et al.* (2002). Figure 10 demonstrates that including the thermodynamic contribution to the first normal stress difference improves the quantitative agreement with measurements of N_1 from rheometry experiments. In addition, table 4 shows that the total first normal stress difference switches in sign from a slightly positive value at $Pe = 0.50$ to an increasingly negative response for $Pe > 1$, also in agreement with Bergenholtz *et al.* (2002).

The coefficients used for the stress-SANS rules for the shear and normal stresses are of the same order of magnitude as those reported by previous works using similar stress-SANS rules for colloidal suspensions (Maranzano & Wagner 2002; Kalman 2010). The coefficients for the thermodynamic shear ($C^{N1,T} = 22$ Pa) and normal stress ($C^{N1,H} = 18$ Pa) contributions are of similar magnitude; see also table 3. The coefficient used to define the first-order hydrodynamic contribution to the stress ($C_0^{\sigma,H} = 0.063$) is significantly smaller owing to the definition of $\overline{W_0}(\dot{\gamma})$, since these values are an order of magnitude larger than those values for $\overline{W_2}(\dot{\gamma})$, $\overline{W_4}(\dot{\gamma})$ and

$\overline{W_{21}}(\dot{\gamma})$. However, the coefficients for the hydrodynamic contribution to the first normal stress ($C^{N1,H} = -5.2$) and the higher-order shear stress ($C_4^{\sigma,H} = 4.6$) are both of the same order of magnitude as each other and opposite in sign, as they should be given the definitions for the shear and first normal stresses in (3.3)–(3.7). At present, there are no theoretical or simulation predictions of these coefficients.

The microscopic viewpoint presented in this paper provides both new insights into suspension rheology as well as a means to test theory and simulation at a more fundamental level than simply the macroscopic properties. Terms of fourth-order symmetry in the microstructure couple to the hydrodynamic interactions to contribute to the stresses and lead to negative first normal stresses and an increasing shear stress in the shear thickened state. This further illustrates that only a few of the components of the structure need to be resolved when considering their effect on the macroscopic stress. Thus, only a small set of microstructure measurements are necessary to critically test simulations and theory. Significantly, the three projections of the microstructure measured by scattering in this work are shown to be able to predict the steady shear thinning and shear thickening states, which has not been demonstrated by any other experimental methods to date.

4. Conclusions

The microstructure of a concentrated near-hard-sphere colloidal dispersion ($\phi_{eff} = 0.465$) is measured for the first time in all three planes of shear using flow- and rheo-SANS experiments. In all three planes the SANS scattering patterns change with increasing shear, indicative of an evolving shear-induced microstructure. Most notable are those measurements made in the velocity–velocity gradient plane of shear in which the signature hydrocluster microstructure of colloidal suspensions is captured in agreement with previous experiments by Kalman (2010) and Stokesian dynamics simulations by Foss & Brady (2000). In addition, SANS scattering results in the velocity–vorticity plane and less so in the velocity gradient–vorticity plane indicate that particles preferentially align along the vorticity direction during strong shearing.

The implementation of the stress-SANS rule successfully predicts the shear and first normal stresses of a concentrated colloidal suspension during steady shear flow from SANS measurements. In addition, using the stress-SANS rule, the thermodynamic and hydrodynamic contributions to the stress are individually defined during steady shear, where the thermodynamic contribution dictates the shear thinning response of the suspension and the hydrodynamic contribution becomes important as the shear rate increases and is ultimately responsible for shear thickening. These results are in agreement with predictions from Stokesian dynamics simulations (Foss & Brady 2000; Banchio & Brady 2003). Here, we find that the leading-order contribution to the shear-induced microstructure is sufficient to define the hydrodynamic contribution to the shear stress for shear rates in the shear thinning regime. However, higher-order microstructure contributions (particularly those with fourfold symmetry in the 1–2 plane of shear) are necessary to define the shear thickening response of the colloidal suspension. Earlier derivations showed the possibility that shear-induced structure with these fourth-order symmetries could couple to the hydrodynamic interactions and thereby contribute to the shear stress. Future advances in rheo-SANS and flow-SANS sample environments as well as SANS diffractometers should enable better resolution of the 3D microstructure across a broader range of shear rates and scattering vectors to better quantify this relationship in the colloidal shear thickened state. Such advances may enable studies of discontinuous shear thickening colloidal

dispersions where and dilatancy becomes evident and the role of other effects, such as interparticle friction, may become important (Brown & Jaeger 2009; Seto *et al.* 2013; Cates & Wyart 2014; Mari *et al.* 2014).

The first normal stress difference is also shown to have contributions from the hydrodynamic and thermodynamic interactions. The contribution to the first normal stress difference from hydrodynamic interactions is predominantly negative and arises only from microstructure with fourfold symmetry, whereas the thermodynamic first normal stress contribution is positive, such that with increasing Pe the total stress contribution switches from a slightly positive value to an increasingly negative response in agreement with theory (Bergenholtz *et al.* 2002) and experiment (Lee *et al.* 2006; Cwalina & Wagner 2014). This observation further confirms that the shear thickened state is dominated by hydrodynamic interactions.

The results presented here show that scattering measurements of the steady shear microstructure can be used to predict the stress of a shearing concentrated colloidal suspension using stress-SANS rules and including terms of fourth-order symmetry. Importantly, the spherical harmonic expansion of the flowing microstructure and subsequent projection into planes of observation provide a robust framework for comparing this and related experimental data directly to future simulation results. Insights gained from examination of the contribution of these structure harmonics to the stresses enables one to focus on the relatively few symmetries that contribute to the shear rheology. Future work will show how colloidal suspensions respond and shear thicken under dynamic oscillatory shear flow by applying the stress-SANS relationships developed herein to microstructure measurements from SANS experiments performed under large-amplitude oscillatory shear.

Acknowledgements

Dr A. P. R. Eberle (Center for Neutron Research, NIST) and Dr L. Porcar (ILL, Grenoble) are gratefully acknowledged for their assistance with the experiments. This manuscript was prepared under cooperative agreements 70NANB7H6178 and 70NANB10H256 from NIST and the US Department of Commerce. A.K.G. acknowledges support from the Delaware Space Grant College and Fellowship Program (NASA grant NNX10AN63H).

Supplementary data

Supplementary data are available at http://dx.doi.org/10.1017/jfm.2015.128.

Appendix A. Hydrodynamic stresses in real space

The complementary expressions for the hydrodynamic stresses expressed as a spherical harmonic expansion in real space are presented here to facilitate the analysis of simulation and direct microscopy measurements of the microstructure. The starting point is the exact expression for the hydrodynamic stresses in the limit of pairwise interactions as given by Batchelor & Green (1972):

$$\sigma_{ij}^{H} = \mu[2 + 5\phi(1+\phi) + 5.4\phi^2]E_{ij} + 5\phi\rho\mu \int_{r\geqslant 2}^{\infty} \left[\frac{\sigma_{ij}^{Hydro}}{\frac{20}{3}\pi a^3 \mu} - E_{ij} \right] h(\boldsymbol{r})\, \mathrm{d}\boldsymbol{r}, \qquad (A\,1)$$

where the hydrodynamic interactions are given as

$$\frac{\sigma_{ij}^{Hydro}}{\frac{20}{3}\pi a^3\mu} - E_{ij} = K(r)E_{ij} + L(r)E_{kl}\left[\frac{r_i r_j I_{jl} + r_j r_k I_{il}}{r^2} - \frac{2}{3}\frac{r_k r_l}{r^2}I_{ij}\right] + M(r)E_{kl}\left[\frac{r_k r_l}{r^2}\left(\frac{r_i r_j}{r^2} - \frac{1}{3}\frac{r_k r_l}{r^2}I_{ij}\right)\right]. \tag{A 2}$$

The structure can be expanded in an expansion in spherical harmonics in a manner complementary to (3.1):

$$\begin{aligned} h(\boldsymbol{r}) = {} & 2B^+_{0,0}(r)Y_{0,0} + 2B^+_{2,0}(r)Y_{2,0} + B^+_{2,1}(r)(Y_{2,-1} - Y_{2,1}) + B^+_{2,2}(r)(Y_{2,2} + Y_{2,-2}) \\ & + 2B^+_{4,0}(r)Y_{4,0} + B^+_{4,1}(r)(Y_{4,-1} - Y_{4,1}) + B^+_{4,2}(r)(Y_{4,2} + Y_{4,-2}) \\ & + B^+_{4,3}(r)(Y_{4,-3} - Y_{4,3}) + B^+_{4,4}(r)(Y_{4,4} + Y_{4,-4}) + \cdots \quad (l \geqslant 6). \end{aligned} \tag{A 3}$$

Note that terms odd in the l index do not appear by symmetry and that terms of $l \geqslant 6$ are not important for the calculation of the stress, as the hydrodynamic stress has terms only up to fourth-order symmetry.

Inserting this expansion into the stress expression and integrating over the angles yields the following terms for the stress components:

$$\begin{aligned} \frac{\sigma^H}{\mu\dot{\gamma}} = {} & [2 + 5\phi(1+\phi) + 5.4\phi^2] + \phi^2\frac{15}{4\pi}\int_{r\geqslant 2}^{\infty}\left[K(r)4\sqrt{\pi}B^+_{0,0}(r)\right. \\ & + L(r)\left(\frac{8\sqrt{\pi}}{3}B^+_{0,0}(r) - \frac{4}{3}\sqrt{\frac{\pi}{5}}B^+_{2,0}(r)\right) + M(r)\left(\frac{4\sqrt{\pi}}{15}B^+_{0,0}(r)\right. \\ & \left.\left. + \frac{4}{21}\sqrt{\frac{\pi}{5}}B^+_{2,0}(r) - \frac{16\sqrt{\pi}}{105}B^+_{4,0}(r) + \frac{4}{21}\sqrt{\frac{2\pi}{5}}B^+_{4,2}(r)\right)\right] r^2\,\mathrm{d}r, \end{aligned} \tag{A 4}$$

$$\frac{N_1^H}{\mu\dot{\gamma}} = \phi^2\frac{15}{4\pi}\int_{r\geqslant 2}^{\infty}\left[M(r)\left(-\frac{4}{3}\sqrt{\frac{\pi}{5}}B^+_{4,1}(r) + \frac{4}{3}\sqrt{\frac{\pi}{35}}B^+_{4,3}(r)\right)\right] r^2\,\mathrm{d}r, \tag{A 5}$$

$$\begin{aligned} \frac{N_2^H}{\mu\dot{\gamma}} = {} & \phi^2\frac{15}{4\pi}\int_{r\geqslant 2}^{\infty}\left[L(r)4\sqrt{\frac{2\pi}{15}}B^+_{2,1}(r)\right. \\ & \left. + M(r)\left(\frac{8}{7}\sqrt{\frac{2\pi}{15}}B^+_{2,1}(r) + \frac{4\sqrt{5\pi}}{21}B^+_{4,1}(r) + \frac{4}{3}\sqrt{\frac{\pi}{35}}B^+_{4,3}(r)\right)\right] r^2\,\mathrm{d}r. \end{aligned} \tag{A 6}$$

These equations can be directly compared to those given in reciprocal space (equations (3.5)–(3.7)), and inspection shows that the same structural symmetries appear in each rheological function. This must be true by the orthogonality properties of spherical harmonics and the symmetry between real and reciprocal space, which is evident from the definitions

$$h(\boldsymbol{k}) = S(\boldsymbol{k}) - 1 = \rho\int h(\boldsymbol{r})\mathrm{e}^{\mathrm{i}\boldsymbol{k}\cdot\boldsymbol{r}}\,\mathrm{d}\boldsymbol{r}, \tag{A 7}$$

$$h(\boldsymbol{r}) = g(\boldsymbol{r}) - 1 = \frac{1}{\rho(2\pi)^3}\int h(\boldsymbol{k})\mathrm{e}^{-\mathrm{i}\boldsymbol{k}\cdot\boldsymbol{r}}\,\mathrm{d}\boldsymbol{k} \tag{A 8}$$

and the Rayleigh expansion

$$\exp(-\mathrm{i}\boldsymbol{k}\cdot\boldsymbol{r}) = \sum_{l,m}(-\mathrm{i})^l \mathrm{j}_l(kr) Y_{l,m}(\Omega_k) * Y_{l,m}(\Omega_r), \tag{A 9}$$

where j_l is the spherical Bessel function of lth order. Therefore, the coefficients are related as

$$B^+_{l,m}(r) = \frac{(-\mathrm{i})^l 2}{3\pi\phi} \int \mathrm{j}_l(kr) B^+_{l,m}(k) k^2 \,\mathrm{d}k \tag{A 10}$$

and

$$B^+_{l,m}(k) = \frac{(\mathrm{i})^l \phi}{3} \int \mathrm{j}_l(kr) B^+_{l,m}(r) r^2 \,\mathrm{d}r. \tag{A 11}$$

This result provides a method to compare the structural coefficients of the spherical harmonic expansion in reciprocal space to those in real space.

REFERENCES

ACKERSON, B. J., HAYTER, J. B., CLARK, N. A. & COTTER, L. 1986 Neutron scattering from charge stabilized suspensions undergoing shear. *J. Chem. Phys.* **84** (1), 2344–2349.

BANCHIO, A. J. & BRADY, J. F. 2003 Accelerated Stokesian dynamics: Brownian motion. *J. Chem. Phys.* **118** (22), 10323–10332.

BARNES, H. A. 1989 Shear-thickening ('dilatancy') in suspensions of nonaggregating solid particles dispersed in Newtonian liquids. *J. Rheol.* **33**, 329–366.

BATCHELOR, G. K. 1977 Effect of Brownian motion on bulk stress in a suspension of spherical particles. *J. Fluid Mech.* **83**, 97–117.

BATCHELOR, G. K. & GREEN, J. T. 1972 The determination of the bulk stress in a suspension of spherical particles to order c^2. *J. Fluid Mech.* **56**, 401–427.

BENDER, J. W. & WAGNER, N. J. 1995 Optical measurement of the contributions of colloidal forces to the rheology of concentrated suspensions. *J. Colloid Interface Sci.* **172** (1), 171–184.

BENDER, J. & WAGNER, N. J. 1996 Reversible shear thickening in monodisperse and bidisperse colloidal dispersions. *J. Rheol.* **40** (5), 899–916.

BERGENHOLTZ, J., BRADY, J. F. & VICIC, M. 2002 The non-Newtonian rheology of dilute colloidal suspensions. *J. Fluid Mech.* **456**, 239–275.

BESSELING, R., ISA, L., WEEKS, E. R. & POON, W. C. K. 2009 Quantitative imaging of colloidal flows. *Adv. Colloid Interface Sci.* **146** (1), 1–17.

BIAN, X., LITVINOV, S., ELLERO, M. & WAGNER, N. J. 2014 Hydrodynamic shear thickening of particulate suspension under confinement. *J. Non-Newtonian Fluid Mech.* **213**, 39–49.

BOSSIS, G. & BRADY, J. F. 1989 The rheology of Brownian suspensions. *J. Chem. Phys.* **91** (3), 1866–1874.

BRADY, J. F. & BOSSIS, G. 1985 The rheology of concentrated suspensions of spheres in simple shear flow by numerical simulation. *J. Fluid Mech.* **155**, 105–129.

BRADY, J. F. & BOSSIS, G. 1988 Stokesian dynamics. *Annu. Rev. Fluid Mech.* **20**, 111–157.

BRADY, J. F. & VICIC, M. 1995 Normal stresses in colloidal dispersions. *J. Rheol.* **39** (3), 545–566.

BROWN, E. & JAEGER, H. M. 2009 Dynamic jamming point for shear thickening suspensions. *Phys. Rev. Lett.* **108** (8), 86001.

CATES, M. E. & WYART, M. 2014 Granulation and bistability in non-Brownian suspensions. *Rheol. Acta* **53** (10), 755–764.

CHENG, X., MCCOY, J. H., ISRAELACHVILI, J. N. & COHEN, I. 2011*a* Imaging the microscopic structure of shear thinning and thickening colloidal suspensions. *Science* **333**, 1276–1279.

CHENG, X., XU, X., RICE, S. A., DINNER, A. R. & COHEN, I. 2011*b* Assembly of vorticity-aligned hard-sphere colloidal strings in a simple shear flow. *Proc. Natl Acad. Sci. USA* **109** (1), 63–67.

COHEN, I., MASON, T. G. & WEITZ, D. A. 2004 Shear-induced configurations of confined colloidal suspensions. *Phys. Rev. Lett.* **93** (4), 046001.

CRAWFORD, N. C., WILLIAMS, S. K. R., BOLDRIDGE, D. & LIBERATORE, M. W. 2013 Shear-induced structures and thickening in fumed silica slurries. *Langmuir* **29** (42), 12915–12923.

CWALINA, C. D. & WAGNER, N. J. 2014 Material properties of the shear-thickened state in concentrated near hard-sphere colloidal dispersions. *J. Rheol.* **58** (4), 949–967.

DAVID, N. V., GAO, X.-L. & ZHENG, J. Q. 2009 Ballistic resistant body armor contemporary and prospective materials and related protection mechanisms. *Appl. Mech. Rev.* **62**, 050802.

DEWHURST, C. 2011 GRASP (program for MATLAB). Institut Laue-Langevin, Grenoble, France.

D'HAENE, P., MEWIS, J. & FULLER, G. G. 1993 Scattering dichroism measurements of flow-induced structure of a shear thickening suspension. *J. Colloid Interface Sci.* **156** (2), 350–358.

FISCHER, C., PLUMMER, C. J. G., MICHAUD, V., BOURBAN, P.-E. & MANSON, J.-A. E. 2007 Pre- and post-transition behavior of shear-thickening fluids in oscillatory shear. *Rheol. Acta* **46**, 1099–1108.

FOSS, D. R. & BRADY, J. F. 2000 Structure, diffusion and rheology of Brownian suspensions by Stokesian dynamics simulation. *J. Fluid Mech.* **407**, 167–200.

GAO, C., KULKARNI, S. D., MORRIS, J. F. & GILCHRIST, J. F. 2010 Direct investigation of anisotropic suspension structure in pressure-driven flow. *Phys. Rev.* E **81**, 041403.

GURNON, A. K. 2014 Nonlinear oscillatory rheology and structure of wormlike micellar solutions and colloidal suspensions. PhD thesis, University of Delaware.

GURNON, A. K., GODFRIN, P. D., EBERLE, A. P. R., BUTLER, P. D. & WAGNER, N. J. 2014 Measuring material microstructure under flow using 1–2 plane flow–small angle neutron scattering. *J. Vis. Exp.* **84**, e51068.

HELBER, R., DONCKER, F. & BUNG, R. 1990 Vibration attenuation by passive stiffness switching mounts. *J. Sound Vib.* **138** (1), 47–57.

HENDERSON, S., MITCHELL, S. & BARTLETT, P. 2001 Direct measurement of colloidal friction coefficients. *Phys. Rev.* E **64**, 061403.

HOEKSTRA, H., MEWIS, J., NARAYANAN, T. & VERMANT, J. 2005 Multi length scale analysis of the microstructure in sticky sphere dispersions during shear flow. *Langmuir* **21** (1), 11017–11025.

HOFFMAN, R. L. 1974 Discontinuous and dilatant viscosity behavior in concentrated suspensions II. Theory and experimental tests. *J. Colloid Interface Sci.* **46**, 491–506.

JOHNSON, S. J., DEKRUIF, C. G. & MAY, R. P. 1988 Structure factor distortion for hardsphere dispersions subjected to weak shear flow: small angle neutron scattering in the flow–vorticity plane. *J. Chem. Phys.* **89** (9), 5910–5921.

KALMAN, D. P. 2010 Microstructure and rheology of concentrated suspensions of near hard-sphere colloids. PhD thesis, University of Delaware.

KALMAN, D. P., MERRILL, R. L., WAGNER, N. J. & WETZEL, E. D. 2009 Effect of particle hardness on the penetration behavior of fabrics intercalated with dry particles and concentrated particle–fluid suspensions. *Appl. Mater. Interfaces* **1** (11), 2602–2612.

KALMAN, D. P. & WAGNER, N. J. 2009 Microstructure of shear-thickening concentrated suspensions determined by flow–USANS. *Rheol. Acta* **48** (8), 897–908.

KAPPL, M., HEIM, L., ECKE, S., FARSHCHI, M. & BUTT, H.-J. 2006 Adhesion and friction of single micrometer-sized particles. In *Detection, Adhesion and Removal* (ed. K. L. Mittal), Particles on Surfaces, vol. 9, pp. 199–210. VSP BV.

KRISHNAMURTHY, L. N., WAGNER, N. J. & MEWIS, J. 2005 Shear thickening in polymer stabilized colloidal dispersions. *J. Rheol.* **49** (6), 1347–1360.

DEKRUIF, C. G., VAN DER WERFF, J. C. & JOHNSON, S. J. 1990 Small-angle neutron-scattering of sheared concentrated dispersions – microstructure along principal flow axes. *Phys. Fluids* A **2** (9), 1545–1556.

LAUN, H. M., BUNG, R., HESS, S., LOOSE, W., HAHN, K., HADICKE, E., HINGMANN, R., SCHMIDT, F. & LINDNER, P. 1992 Rheological and small-angle neutron scattering investigation of shear-induced particle structures of concentrated polymer dispersions submitted to plane Poiseuille and Couette flow. *J. Rheol.* **36** (4), 743–787.

LEE, M., ALCOUTLABI, M., MAGDA, J. J., DIBBLE, C., SOLOMON, M. J., SHI, X. & MCKENNA, G. B. 2006 The effect of the shear-thickening transition of model colloidal spheres on the sign of N_1 and on the radial pressure profile in torsional shear flows. *J. Rheol.* **50** (3), 293–311.

LEE, Y. S. & WAGNER, N. J. 2006 Rheological properties and small-angle neutron scattering of a shear thickening nanoparticle dispersion at high shear rates. *Ind. Engng Chem. Res.* **46** (1), 7015–7024.

LEE, Y. S., WETZEL, E. D. & WAGNER, N. J. 2003 The ballistic impact characteristics of Kevlar woven fabrics impregnated with a colloidal shear thickening fluid. *J. Mater. Sci.* **38**, 2825–2833.

LIM, A. S., LOPATNIKOV, S. L., WAGNER, N. J. & GILLESPIE, J. W. 2010*a* An experimental investigation into the kinematics of a concentrated hard-sphere colloidal suspension during Hopkinson bar evaluation at high stresses. *J. Non-Newtonian Fluid Mech.* **165** (19–20), 1342–1350.

LIM, A. S., LOPATNIKOV, S. L., WAGNER, N. J. & GILLESPIE, J. W. 2010*b* Investigating the transient response of a shear thickening fluid using the split Hopkinson pressure bar technique. *Rheol. Acta* **49** (8), 879–890.

LIM, A. S., LOPATNIKOY, S. L., WAGNER, N. J. & GILLESPIE, J. W. 2011 Phenomenological modeling of the response of a dense colloidal suspension under dynamic squeezing flow. *J. Non-Newtonian Fluid Mech.* **166** (12–13), 680–688.

MARANZANO, B. J. 2001 Rheology and microstructure of concentrated near hard sphere colloidal dispersions at the shear thickening transition. PhD thesis, University of Delaware.

MARANZANO, B. J. & WAGNER, N. J. 2002 Flow-small angle neutron scattering measurements of colloidal dispersion microstructure evolution through the shear thickening transition. *J. Phys. Chem.* **117** (22), 10291–10302.

MARI, R., SETO, R., MORRIS, J. F. & DENN, M. M. 2014 Shear thickening, frictionless and frictional rheologies in non-Brownian suspensions. *J. Rheol.* **58**, 1693–1724.

MELROSE, J. R. & BALL, R. C. 2004 Continuous shear thickening transitions in model concentrated colloids – the role of interparticle forces. *J. Rheol.* **48** (5), 937–960.

MEWIS, J. & WAGNER, N. J. 2011 *Colloidal Suspension Rheology*. Cambridge University Press.

MORRIS, J. D. & BOULAY, F. 1999 Curvilinear flows of noncolloidal suspensions: the role of normal stresses. *J. Rheol.* **43**, 1213–1237.

MUTHIG, M., PREVOST, S., ORGLEMEISTER, R. & GRADZIELSKI, M. 2013 SASET: a program for series analysis of small-angle scattering data. *J. Appl. Crystallogr.* **46**, 1187–1195.

NAZOCKDAST, E. & MORRIS, J. F. 2013 Pair-particle dynamics and microstructure in sheared colloidal suspensions: simulation and Smoluchowski theory. *Phys. Fluids* **25** (7), 070601.

NEWSTEIN, M. C., WANG, H., BALSARA, N. P., LEFEBVRE, A. A., SHNIDMAN, Y., WATANABE, H., OSAKI, K., SHIKATA, T., NIWA, H. & MORISHIMA, Y. 1999 Microstructural changes in a colloidal liquid in the shear thinning and shear thickening regimes. *J. Chem. Phys.* **111** (10), 4827–4838.

PHUNG, T. N., BRADY, J. F. & BOSSIS, G. 1996 Stokesian dynamics simulation of Brownian suspensions. *J. Fluid Mech.* **313**, 181–207.

PORCAR, L., POZZO, D., LANGENBUCHER, G., MOYER, J. & BUTLER, P. D. 2011 Rheo small-angle neutron scattering at the National Institute of Standards and Technology Center for Neutron Research. *Rev. Sci. Instrum.* **82**, 0830902.

RAVIV, U., GIASSON, S., KAMPF, N., GOHY, J. F., JEROME, R. & KLEIN, J. 2003 Lubrication by charged polymers. *Nature* **425** (6954), 163–165.

RUSSEL, W. B., WAGNER, N. J. & MEWIS, J. 2013 Divergence in the low shear viscosity for Brownian hard-sphere dispersions: at random close packing or the glass transition? *J. Rheol.* **57** (6), 1555–1567.

SETO, R., MARI, R., MORRIS, J. F. & DENN, M. M. 2013 Discontinuous shear thickening of frictional hard-sphere suspensions. *Phys. Rev. Lett.* **111**, 218301.

SHIKATA, T. & PEARSON, D. S. 1994 Viscoelastic behavior of concentrated spherical suspensions. *J. Rheol.* **38** (3), 601–616.

TOUSSAINT, F., ROY, C. & JEZEQUEL, P. H. 2009 Reducing shear thickening of cement-based suspensions. *Rheol. Acta* **48** (8), 883–895.

VERSMOLD, H., MUSA, S. & BIERBAUM, A. 2002 Concentrated colloidal dispersions: on the relation of rheology with small angle x-ray and neutron scattering. *J. Chem. Phys.* **116** (6), 2658–2662.

VERSMOLD, H., MUSA, S., DUX, C., LINDNER, P. & URBAN, V. 2001 Shear-induced structure in concentrated dispersions: small angle synchrotron x-ray and neutron scattering. *Langmuir* **17** (1), 6812–6815.

WAGNER, N. J. & ACKERSON, B. J. 1992 Analysis of nonequilibrium structures of shearing colloidal suspensions. *J. Chem. Phys.* **97**, 1473–1483.

WAGNER, N. J., FULLER, G. G. & RUSSEL, W. B. 1988 The dichroism and birefringence of a hard-sphere suspension under shear. *J. Chem. Phys.* **89** (3), 1580–1587.

WATANABE, H., YAO, M.-L., OSAKI, K., SHIKATA, T., NIWA, H., MORISHIMA, Y., BALSARA, N. P. & WANG, H. 1998 Nonlinear rheology and flow-induced structure in a concentrated spherical silica suspension. *Rheol. Acta* **37** (1), 1–6.

XU, B. & GILCHRIST, J. F. 2014 Microstructure of sheared monosized colloidal suspensions resulting from hydrodynamic and electrostatic interactions. *J. Chem. Phys.* **140**, 204903.

ZHANG, X. Z., LI, W. H. & GONG, X. L. 2008 The rheology of shear thickening fluid (STF) and the dynamic performance of an STF-filled damper. *Smart Mater. Struct.* **17** (1), 035027.